A stable added-mass partitioned (AMP) algorithm for elastic solids and incompressible flow

D. A. Serino[a,4,3], J. W. Banks[a,1,2], W. D. Henshaw[a,1,3], D. W. Schwendeman[a,1,3,*]

[a]*Department of Mathematical Sciences, Rensselaer Polytechnic Institute, Troy, NY 12180, USA*

Abstract

A stable added-mass partitioned (AMP) algorithm is developed for fluid-structure interaction (FSI) problems coupling viscous incompressible flow and compressible elastic solids. The hyperbolic system governing the solid is integrated using an explicit upwind (Godunov) scheme. The equations for the fluid are integrated using an implicit-explicit (IMEX) fractional-step scheme whereby the velocity is advanced in one step, treating the viscous terms implicitly, and the pressure is computed in a second step. The AMP interface conditions for the fluid arise from the outgoing characteristic variables in the solid, and they are partitioned into a Robin (mixed) interface condition for the pressure and interface conditions for the velocity. The latter conditions include an impedance-weighted average between fluid and solid velocities using a fluid impedance of a special form. A similar impedance-weighted average is used to define interface values for the solid. Deforming composite grids are used to effectively handle the evolving geometry and large deformations. The new algorithm is verified for accuracy and stability on a number of useful benchmark problems in two space dimensions, including a radial-piston problem for which exact solutions for radial and azimuthal motions are found and tested. Exact traveling wave solutions for a solid disk surrounded by an annular region of fluid are also derived and used to verify the AMP scheme. Fluid flow in a channel past a deformable solid annulus is computed, and the errors are estimated from a self-convergence grid refinement study. The AMP scheme is found to be stable and second-order accurate, without sub-time-step iterations, even for very difficult cases of very light solids when added-mass and added-damping effects are large.

Keywords: fluid-structure interaction; moving overlapping grids; incompressible Navier-Stokes; partitioned schemes; added-mass and added-damping; elastic solids

1. Introduction

Fluid-structure interaction (FSI) problems involving incompressible fluids and elastic solids occur in many areas of engineering and applied science. Examples include modeling flow-induced vibrations of structures (i.e., aircraft wings, undersea cables, wind turbines, and bridges) and simulating blood flow in arteries and veins. These problems are typically modeled using partial

*Department of Mathematical Sciences, Rensselaer Polytechnic Institute, 110 8th Street, Troy, NY 12180, USA.

Email addresses: serind@rpi.edu (D. A. Serino), banksj3@rpi.edu (J. W. Banks), henshw@rpi.edu (W. D. Henshaw), schwed@rpi.edu (D. W. Schwendeman)

[1]This work was supported by contracts from the U.S. Department of Energy ASCR Applied Math Program.

[2]Research supported by a U.S. Presidential Early Career Award for Scientists and Engineers.

[3]Research supported by the National Science Foundation under grants DMS-1519934 and DMS-1818926.

[4]Research supported by the National Science Foundation Graduate Research Fellowship under Grant No. DGE-1744655.

differential equations for both the fluid and solid in their respective domains together with coupling conditions involving velocity and stress at the fluid-solid interface. FSI problems are challenging mathematically due, in part, to the evolving fluid and solid domains, and the coupling at the moving interface. Numerical algorithms have been developed to compute solutions of the governing equations, and these schemes can be classified broadly as monolithic or partitioned. Monolithic schemes integrate the equations implicitly as a single large system of coupled equations, while partitioned schemes use separate solvers for the fluid and solid together with some approach to couple the solutions at each time step. Partitioned schemes are often preferred for modularity and computational performance, but they can suffer from instabilities associated with the method used to couple the solutions at the interface. For example, a standard traditional partitioned (TP) scheme employs a coupling approach in which the solid provides a Dirichlet (no-slip) boundary condition for the fluid, and then the fluid supplies a Neumann (traction) boundary condition for the solid. This approach is appealing from a physical point of view in the case when the density of the solid is much greater than that of the fluid, but it is well known [1] that TP schemes suffer from *added-mass* instabilities in the case when the solid is *light* relative to the fluid. A method of iteration of the coupling conditions can be included in a TP algorithm in effort to suppress added-mass instabilities, but the effectiveness of this sub-time-step iteration is limited and it increases the cost of the algorithm.

In recent work [2, 3], we developed a new class of Added-Mass Partitioned (AMP) algorithms for FSI problems coupling incompressible flow and elastic solids. The work in [2] for bulk solids and in [3] for thin structures both considered Stokes flow and linear elastic solids, with the fluid-solid interface linearized about a flat surface. The algorithms used a fractional-step approach for the fluid in which the velocity is advanced in one stage followed by the solution of a Poisson problem for the pressure. A key ingredient in the algorithms is the AMP interface conditions, which includes a mixed Robin condition for the pressure. For the case of a bulk solid, this condition includes the *acceleration* of the solid through a consideration of the outgoing characteristic variables of the hyperbolic system for the elastic solid and the interface conditions. The velocity and stress at the interface are set by impedance-weighted averages so that the AMP conditions behave correctly in the limits of heavy and light solids. Thus, the resulting AMP algorithm is stable for *any* ratio of the density of the solid to that of the fluid, without sub-time-step iterations, effectively suppressing added-mass instabilities. In [4], the approach for thin structures was extended to incompressible flows with nonlinear convection and Euler-Bernoulli beams with finite deflection, and it was found that the AMP scheme remains stable for both heavy and light solids.

The aim of the present work is to develop a stable and second-order accurate AMP algorithm for FSI problems coupling incompressible flow and linear elastic bulk solids. The scheme follows the work in [2], but with significant modifications to handle finite deformation of the fluid-solid interface, nonlinear advection in the fluid, an IMEX-type scheme for the fluid, and viscous added-damping effects. The Navier-Stokes equations for the fluid are solved in either an Eulerian frame or an Arbitrary-Eulerian-Lagrangian (ALE) frame which is coupled to the motion of the interface, while the equations governing the solid are solved in a static Lagrangian reference frame. Both the fluid and solid domains are covered by composite overlapping grids [5], with the deformation of the fluid grid performed using the approach described originally in [6]. For example, Figure 1 shows a composite grid for an FSI problem involving a fluid in a channel flowing past three elastic solids in the shape of the letters "R", "P" and "I". The viscous fluid flows from left to right, and it interacts with the three solids whose computed displacements determine the deformed shapes. The image on the far-right of the figure shows an enlarged view of the composite grid near the fluid-solid interface of the right-most deformed solid.

The equations of linear elasticity in the solid domain are advanced explicitly using the time-

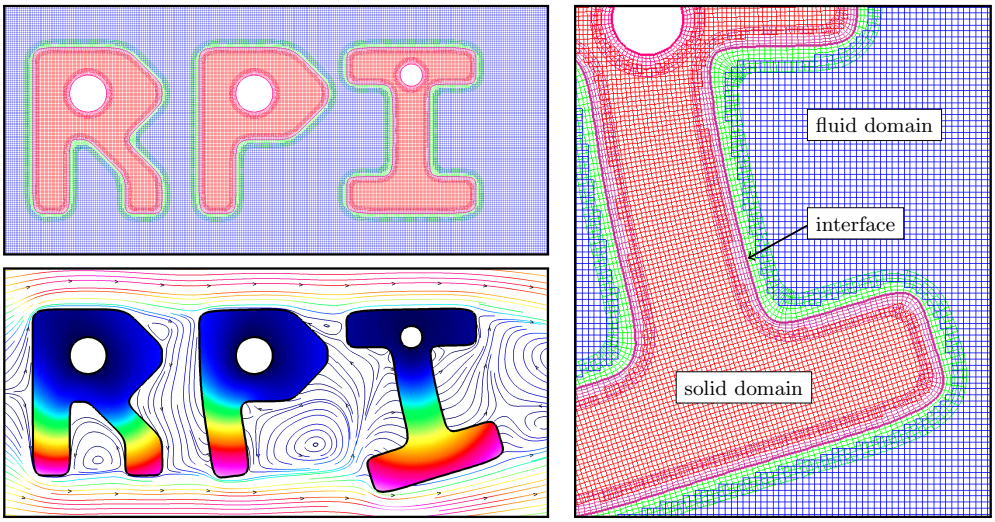

Figure 1: Top left: Initial grid is composed of a (blue) background grid and (green) deforming interface-fitted grids representing the fluid domain. The 'RPI' shaped solid domain is composed of (red) background grids, (purple) interface-fitted grids, and (pink) annular grids around interior cores where the displacement is set to zero. Bottom left: Solution at $t = 15$ described by streamlines in the fluid domain and shaded contours of the magnitude of the solid displacement. Right: Enlarged view of the grid after solid deformation.

stepping scheme described in [7] for the hyperbolic system of equations in first-order form. The Navier-Stokes equations in the fluid domain are solved using a fractional-step scheme. Unlike the earlier work [2], the present solver uses an implicit-explicit (IMEX) scheme based on [8]. In this scheme, the fluid velocity is advanced first with the viscous terms treated implicitly while the pressure gradient and nonlinear convection terms are handled explicitly. The fluid pressure is updated in a subsequent step by solving a Poisson problem. The incorporation of the IMEX scheme has necessitated important changes to the original AMP interface conditions introduced in [2] to handle viscous added-damping effects that arise when the viscous CFL number becomes large. Modifications to the AMP interface conditions are guided by the analysis of carefully chosen FSI model problems, as discussed in the companion manuscript [9] (with additional details found in [10]). In particular, the analysis reveals a stable definition of the fluid impedance, which is a critical ingredient in the present AMP algorithm. Furthermore, in [9] the AMP scheme is shown to be stable for a linearized model problem in two dimensions that couples the incompressible Stokes equations to an elastic solid, while in [10] the scheme is shown to be second-order accurate and stable for a two-dimensional model problem involving an inviscid incompressible fluid and an elastic solid. The focus of the present work is a description of this algorithm for the full FSI problem, and its implementation in two space dimensions using deforming composite grids (DCG). Performance of the algorithm is examined for a set of FSI benchmark problems, including ones in which new exact solutions are derived. These results are used to demonstrate the stability and accuracy of the algorithm, and a comparison to results from a traditional partitioned scheme is also provided.

The overarching technique used to derive Added-Mass Partitioned schemes relies on the use of so-called compatibility boundary conditions, which are derived from the governing PDEs in concert with the interface conditions. This approach has also been used in a variety of other FSI regimes to yield stable and accurate partitioned solvers without the need for sub-iteration. These AMP algorithms, including the one described here, behave as strongly-coupled partitioned schemes (or monolithic schemes) since the interface conditions are satisfied accurately, yet the schemes are stable for any ratio of the fluid and solid densities without the need for sub-iterations. In the case of FSI

problems involving viscous incompressible flow, for example, AMP schemes have been developed for thin elastic structures [4] (as noted above) and for rigid solids [11–13]. The first AMP schemes were developed for compressible flow [14, 15], and were subsequently extended into a general 2D framework using the DCG approach for FSI problems involving inviscid compressible flows and linear elastic solids [5]. For the case of inviscid compressible flow, added-mass effects are localized due to finite propagation speeds of disturbances in the fluid [16], and this leads to a somewhat simpler treatment of the coupling conditions in the corresponding AMP scheme relative to the incompressible case considered here. Extensions of the scheme in [5] to FSI problems coupling inviscid compressible flow and rigid solids is described in [17], with the case of nonlinear elastic solids detailed in [18].

In addition to the work cited above, there are other approaches to addressing added-mass-type instabilities in both partitioned [19–21] and monolithic FSI solvers. For partitioned schemes, a typical strategy is to used under-relaxed sub-iterations, and previous research has shown that the number of necessary sub-iterations can be reduced by the use of Aitken acceleration or quasi-Newton methods, see [22, 23]. Additionally, sub-iteration schemes based on Robin-Neumann or Robin-Robin coupling, as opposed to the traditional Dirichlet-Neumann coupling, have also been shown to yield performance gains [24–33]. In related research, added-mass effects can also be treated by adding fictitious mass terms in the structure equations [34, 35] or artificial compressibility in the fluid equations [36–38] or using a semi-monolithic approach [39]. For difficult problems with large added-mass effects, monolithic schemes have been used to eliminate the need for sub-iterations [40, 41], and the performance of monolithic schemes has improved significantly through the application of multigrid [42–45].

The remaining sections of the paper are organized as follows. The equations governing the FSI problem are described in Section 2, and the AMP algorithm is described in Section 3. In the latter section, we begin with a discussion of the AMP interface conditions at a continuous level, which is followed by a detailed discussion of the AMP scheme. The description of the AMP scheme focuses on the time-stepping of the solid and fluid solvers, and the treatment of the interface conditions, which are independent of the details of the spatial approximations. Section 4 provides a description of the spatial approximations using deforming composite grids (DCG), as shown in Figure 1 for example. Numerical results confirming the stability and accuracy of the scheme and discussed in Section 5. Some of the results use new exact solutions of benchmark FSI problems, which are described in the appendices. Conclusions are given in Section 6.

2. Governing equations and interface conditions

We consider the coupled evolution of an incompressible fluid and a linear elastic solid. The fluid occupies the domain $\mathbf{x} \in \Omega(t)$, where $\mathbf{x} = (x_1, x_2, x_3)$ is a vector of physical coordinates and t is time. The equations for the solid are written in terms of the Lagrangian coordinate $\bar{\mathbf{x}} = (\bar{x}_1, \bar{x}_2, \bar{x}_3)$ for a reference configuration $\bar{\mathbf{x}} \in \bar{\Omega}_0$ at $t = 0$. (An overbar is used here and elsewhere to denote quantities associated with the solid.) The fluid and solid are coupled at an interface described by $\mathbf{x} \in \Gamma(t)$ in physical space and $\bar{\mathbf{x}} \in \bar{\Gamma}_0$ in the corresponding reference space. Figure 1 illustrates these geometric features using a model fluid-structure interaction problem.

The fluid is described by the incompressible Navier-Stokes equations

$$\nabla \cdot \mathbf{v} = 0, \qquad \mathbf{x} \in \Omega(t), \tag{1a}$$

$$\rho \mathbf{v}_t + \rho(\mathbf{v} \cdot \nabla)\mathbf{v} = \nabla \cdot \boldsymbol{\sigma}, \qquad \mathbf{x} \in \Omega(t), \tag{1b}$$

where $\mathbf{v}(\mathbf{x},t)$ is the velocity, $\boldsymbol{\sigma}(\mathbf{x},t)$ is the stress tensor and ρ is the (constant) density. The fluid stress tensor is given by

$$\boldsymbol{\sigma} = -p\mathbf{I} + \boldsymbol{\tau}, \tag{2}$$

where $p(\mathbf{x},t)$ is the pressure, $\mathbf{I}$ is the identity matrix and $\boldsymbol{\tau}(\mathbf{x},t)$ is the viscous stress tensor. The latter quantity is given in terms of the gradient of the fluid velocity by

$$\boldsymbol{\tau} = \mu\left(\nabla\mathbf{v} + (\nabla\mathbf{v})^T\right), \tag{3}$$

where μ is the dynamic viscosity of the fluid (assumed to be constant).

We consider the governing equations for the fluid in velocity-pressure form. In this form, the continuity equation in (1a) is replaced by a Poisson equation for the pressure given by

$$\Delta p = -\rho\nabla\mathbf{v} : (\nabla\mathbf{v})^T, \qquad \mathbf{x} \in \Omega(t), \tag{4}$$

where

$$\nabla\mathbf{v} : (\nabla\mathbf{v})^T \equiv \sum_{i=1}^{3}\sum_{j=1}^{3} \frac{\partial v_i}{\partial x_j}\frac{\partial v_j}{\partial x_i}.$$

Here, components of the fluid velocity $\mathbf{v}$ are denoted by (v_1, v_2, v_3), and a similar notation is used for the components of tensors, e.g. the components of $\boldsymbol{\sigma}$ are given by σ_{mn} with $m, n = 1$, 2, 3. In the velocity-pressure form of the equations, boundary conditions are required for the the pressure-Poisson equation. A suitable choice that ensures consistency with solutions of the velocity-divergence form is $\nabla \cdot \mathbf{v} = 0$ for $\mathbf{x} \in \partial\Omega(t)$.

The evolution of the solid is described by the equations of linear elasticity. These equations can be written in the form

$$\bar{\mathbf{u}}_t = \bar{\mathbf{v}}, \qquad \bar{\mathbf{x}} \in \bar{\Omega}_0, \tag{5a}$$

$$\bar{\rho}\bar{\mathbf{v}}_t = \nabla_{\bar{\mathbf{x}}} \cdot \bar{\boldsymbol{\sigma}}, \qquad \bar{\mathbf{x}} \in \bar{\Omega}_0, \tag{5b}$$

where $\bar{\mathbf{u}}(\bar{\mathbf{x}},t)$ is the displacement of the solid, $\bar{\mathbf{v}}(\bar{\mathbf{x}},t)$ its velocity, and $\bar{\rho}$ its density (assumed constant). The Cauchy stress tensor $\bar{\boldsymbol{\sigma}}(\bar{\mathbf{x}},t)$ in (5b) is defined by

$$\bar{\boldsymbol{\sigma}} = \bar{\lambda}(\nabla_{\bar{\mathbf{x}}} \cdot \bar{\mathbf{u}})\mathbf{I} + \bar{\mu}\left(\nabla_{\bar{\mathbf{x}}}\bar{\mathbf{u}} + (\nabla_{\bar{\mathbf{x}}}\bar{\mathbf{u}})^T\right), \tag{6}$$

where $\bar{\lambda}$ and $\bar{\mu}$ are Lamé parameters (taken to be constants). The position of the solid in physical space is determined by the mapping

$$\mathbf{x} = \bar{\mathbf{x}} + \bar{\mathbf{u}}(\bar{\mathbf{x}},t), \tag{7}$$

for $\bar{\mathbf{x}} \in \bar{\Omega}_0$. The corresponding deformation gradient given by $\bar{F} = \nabla_{\bar{\mathbf{x}}}\mathbf{x} = \mathbf{I} + \nabla_{\bar{\mathbf{x}}}\bar{\mathbf{u}}$ is assumed to be a small perturbation of the identity for a linear elastic solid so that a one-to-one mapping from the reference space to the physical space of the solid exists. Following the approach described in [7], the solid equations are treated as a first order system of PDEs in time and space. This formulation is achieved by taking the time derivative of (6) to obtain

$$\bar{\boldsymbol{\sigma}}_t = \bar{\lambda}(\nabla_{\bar{\mathbf{x}}} \cdot \bar{\mathbf{v}})\mathbf{I} + \bar{\mu}\left(\nabla_{\bar{\mathbf{x}}}\bar{\mathbf{v}} + (\nabla_{\bar{\mathbf{x}}}\bar{\mathbf{v}})^T\right), \qquad \bar{\mathbf{x}} \in \bar{\Omega}_0, \tag{8}$$

which is then appended to previous system of equations in (5). In this form, upwind solvers can be used to advance displacement, velocity and stress of the solid. We note that (6) is enforced at $t = 0$, and then the stress-strain relation is satisfied approximately for $t > 0$ through compatibility conditions applied at the boundary and a stress-strain relaxation term in the numerical scheme (see [18]).

The interface between the fluid and solid, in physical space given by $\mathbf{x} \in \Gamma(t)$, is determined by the mapping in (7) for the boundary of the solid given by $\bar{\mathbf{x}} \in \bar{\Gamma}_0$. The interface is assumed to be smooth so that a well-defined normal to the interface exists. Along the interface, the following matching conditions hold:

$$\mathbf{v} = \bar{\mathbf{v}}, \qquad \mathbf{x} \in \Gamma(t), \tag{9a}$$

$$\boldsymbol{\sigma}\mathbf{n} = \bar{\boldsymbol{\sigma}}\mathbf{n}, \qquad \mathbf{x} \in \Gamma(t), \tag{9b}$$

where $\mathbf{n}(\mathbf{x}, t)$ is the outward unit normal to the fluid domain, i.e. $\mathbf{n}$ points from the fluid domain to the solid domain. Suitable boundary conditions are applied on the boundaries of the fluid and solid domians not included in $\Gamma(t)$, and initial conditions on $\mathbf{v}$, $\bar{\mathbf{u}}$ and $\bar{\mathbf{v}}$ are set to close the problem.

Since the equations governing the solid form a hyperbolic system, it is informative to consider the propagation of characteristics. The primary and secondary wave speeds are defined as

$$\bar{c}_p = \sqrt{\frac{\bar{\lambda} + 2\bar{\mu}}{\bar{\rho}}}, \qquad \bar{c}_s = \sqrt{\frac{\bar{\mu}}{\bar{\rho}}}, \tag{10}$$

which correspond to compression and sheer waves, respectively. At the interface, the Riemann variables corresponding to incoming and outgoing characteristics can be obtained from the first-order equations in (5b) and (8) projected onto the normal to the interface. These variables for the compression and shear waves are given by

$$\mathcal{A}(\bar{\boldsymbol{\sigma}}, \bar{\mathbf{v}}) = \mathbf{n}^T\bar{\boldsymbol{\sigma}}\mathbf{n} - \bar{z}_p\mathbf{n}^T\bar{\mathbf{v}}, \qquad \mathbf{x} \in \Gamma(t) \quad \text{(incoming)}, \tag{11a}$$

$$\mathcal{A}_m(\bar{\boldsymbol{\sigma}}, \bar{\mathbf{v}}) = \mathbf{t}_m^T\bar{\boldsymbol{\sigma}}\mathbf{n} - \bar{z}_s\mathbf{t}_m^T\bar{\mathbf{v}}, \quad m = 1, 2, \qquad \mathbf{x} \in \Gamma(t) \quad \text{(incoming)}, \tag{11b}$$

corresponding to information propagating into the solid domain, and

$$\mathcal{B}(\bar{\boldsymbol{\sigma}}, \bar{\mathbf{v}}) = \mathbf{n}^T\bar{\boldsymbol{\sigma}}\mathbf{n} + \bar{z}_p\mathbf{n}^T\bar{\mathbf{v}}, \qquad \mathbf{x} \in \Gamma(t) \quad \text{(outgoing)}, \tag{11c}$$

$$\mathcal{B}_m(\bar{\boldsymbol{\sigma}}, \bar{\mathbf{v}}) = \mathbf{t}_m^T\bar{\boldsymbol{\sigma}}\mathbf{n} + \bar{z}_s\mathbf{t}_m^T\bar{\mathbf{v}}, \quad m = 1, 2, \qquad \mathbf{x} \in \Gamma(t) \quad \text{(outgoing)}, \tag{11d}$$

corresponding to information propagating out of the solid domain. Here, $\mathbf{t}_1(\mathbf{x}, t)$ and $\mathbf{t}_2(\mathbf{x}, t)$ are mutually orthogonal unit vectors tangent to $\Gamma(t)$, and thus orthogonal to $\mathbf{n}$, and $\bar{z}_p = \bar{\rho}\bar{c}_p$ and $\bar{z}_s = \bar{\rho}\bar{c}_s$ are the solid impedances for compression and shear waves, respectively. The functions given in (11), corresponding to the Riemann variables for the solid, can be used to derive an equivalent set of characteristic-based interface conditions which take into account the direction of propagation. These conditions are

$$\mathcal{A}(\bar{\boldsymbol{\sigma}}, \bar{\mathbf{v}}) = \mathcal{A}(\boldsymbol{\sigma}, \mathbf{v}), \qquad \mathcal{A}_m(\bar{\boldsymbol{\sigma}}, \bar{\mathbf{v}}) = \mathcal{A}_m(\boldsymbol{\sigma}, \mathbf{v}), \qquad \mathbf{x} \in \Gamma(t), \tag{12a}$$

$$\mathcal{B}(\boldsymbol{\sigma}, \mathbf{v}) = \mathcal{B}(\bar{\boldsymbol{\sigma}}, \bar{\mathbf{v}}), \qquad \mathcal{B}_m(\boldsymbol{\sigma}, \mathbf{v}) = \mathcal{B}_m(\bar{\boldsymbol{\sigma}}, \bar{\mathbf{v}}), \qquad \mathbf{x} \in \Gamma(t), \tag{12b}$$

which are linear combinations of the matching conditions in (9).

This paper is concerned with partitioned algorithms for solving FSI problems involving incompressible fluids and linear elastic solids. Such algorithms employ PDE solvers for the equations governing the fluid and solid separately with the matching conditions at the fluid-solid interface

providing boundary conditions for each domain solver (along with conditions on the boundaries not included in the shared interface). For example, in traditional partitioned algorithms, the fluid velocity is determined by the solid, while the solid traction is determined by the fluid. This ordering can often be used for the case of heavy solids, but it suffers from added-mass instabilities when the solid density is light or the solid grid is very fine. In the reverse scheme, referred to as the anti-traditional scheme, the solid imposes a traction condition on the fluid, while the fluid velocity provides a condition for the solid velocity. This reverse ordering works well for light solids or fine grids, but may exhibit instability for heavy solids or coarse grids.

The added-mass partitioned (AMP) scheme described in the next section follows the work in [2], and uses the characteristic-based matching conditions in (12). At a high level, these are implemented as boundary conditions for the solid solver as

$$\mathcal{A}(\bar{\boldsymbol{\sigma}}, \bar{\mathbf{v}}) = \mathcal{A}(\boldsymbol{\sigma}^{(p)}, \mathbf{v}^{(p)}), \qquad \mathcal{A}_m(\bar{\boldsymbol{\sigma}}, \bar{\mathbf{v}}) = \mathcal{A}_m(\boldsymbol{\sigma}^{(p)}, \mathbf{v}^{(p)}), \qquad \mathbf{x} \in \Gamma(t), \tag{13a}$$

and as boundary conditions for the fluid solver as

$$\mathcal{B}(\boldsymbol{\sigma}, \mathbf{v}) = \mathcal{B}(\bar{\boldsymbol{\sigma}}^{(p)}, \bar{\mathbf{v}}^{(p)}), \qquad \mathcal{B}_m(\boldsymbol{\sigma}, \mathbf{v}) = \mathcal{B}_m(\bar{\boldsymbol{\sigma}}^{(p)}, \bar{\mathbf{v}}^{(p)}), \qquad \bar{\mathbf{x}} \in \Gamma(t), \tag{13b}$$

where the (p) superscript denotes suitable *predicted* values (as described in more detail below) so that the right-hand sides of the boundary conditions in (13) are treated as known. This characteristic-based decomposition of the interface matching conditions is a key step in the derivation of the AMP algorithm, and it leads to a stable scheme for a wide range of fluid and solid densities. In particular, in the limits of heavy solids and light solids, the AMP scheme approaches the traditional and anti-traditional partitioned schemes, respectively.

3. FSI algorithms

In this section, we describe the AMP algorithm, and we also discuss the traditional partitioned (TP) algorithm and the anti-traditional partitioned (ATP) algorithm for comparative purposes. The ATP algorithm uses a reverse coupling scheme in which the fluid provides a Dirichlet (velocity) boundary condition for the solid, and then the solid supplies a Neumann (stress) boundary condition for the fluid. All three partitioned schemes use the same fluid and solid domain solvers. For the fluid domain, we integrate the governing equations in velocity-pressure form using a fractional-step scheme in which the fluid velocity is advanced in one step and the pressure-Poisson equation is solved to update the fluid pressure in the other step (see [8]). An explicit upwind Godunov method is used to advance the velocity and stress of the solid in its reference domain following the approach described in [7], while a Lax-Wendroff scheme is used to advance the solid displacement. These two domain solvers, both second-order accurate in space and time, are embedded in the FSI algorithms using a predictor-corrector approach. The first step of the FSI time-stepping loop involves advancing the solid variables to the next time level. The solid displacement predicts the new position of the fluid-solid interface and this information is used to deform the fluid grid and compute its *grid velocity*. The fluid-domain solver is then called to advance the fluid velocity to the next time level and update the fluid pressure. In the fluid solver, the diffusion terms of the momentum equations are treated implicitly, while the convection and pressure-gradient terms are approximated explicitly. Following this fluid-domain step, the solid interface data is updated using fluid data at the new time level. The steps outlined above are essentially repeated in the corrector step. Depending on the densities of the fluid and solid (and on the grid spacing), the TP and ATP schemes may require addition sub-iterations for stability, in which case the corrector step is repeated.

The AMP algorithm differs from that of the TP and ATP schemes in the implementation of the fluid-solid interface conditions. To this end, we begin in Section 3.1 by describing the various treatments of the interface conditions, including compatibility conditions, at a continuous level. This discussion is then followed in Section 3.2 by a detailed description of the various FSI algorithms at a discrete level.

3.1. Continuous interface conditions

Using the formulas for the fluid stress tensor in (2) and (3), the AMP interface conditions in (13b) for the fluid become

$$-p + \mathbf{n}^T\boldsymbol{\tau}\mathbf{n} + \bar{z}_p\mathbf{n}^T\mathbf{v} = \mathbf{n}^T\bar{\boldsymbol{\sigma}}\mathbf{n} + \bar{z}_p\mathbf{n}^T\bar{\mathbf{v}}, \qquad \mathbf{x}\in\Gamma(t), \tag{14a}$$

$$\mathbf{t}_m^T\boldsymbol{\tau}\mathbf{n} + \bar{z}_s\mathbf{t}_m^T\mathbf{v} = \mathbf{t}_m^T\bar{\boldsymbol{\sigma}}\mathbf{n} + \bar{z}_s\mathbf{t}_m^T\bar{\mathbf{v}}, \quad m=1,2, \qquad \mathbf{x}\in\Gamma(t), \tag{14b}$$

with the (p) superscript on the solid variables suppressed. These conditions, along with $\nabla\cdot\mathbf{v}=0$ applied on the boundary, are a sufficient set of conditions for the fluid equations in velocity-pressure form. The left-hand side of the interface conditions in (14b) only involve the fluid velocity (and its derivatives), and these conditions with the divergence-free constraint (which acts as a Neumann-type condition for the normal component of the velocity) are used as boundary conditions for the momentum equation in (1b) to advance the fluid velocity. The stress and velocity of the solid appearing on the right-hand side of (14b) are obtained from an explicit time step of the hyperbolic system of equations for the solid. Once the fluid velocity is advanced to the next time step, a Poisson problem is solved to update the fluid pressure. Following the analysis in [2, 9], the interface condition in (14a) is used with the momentum equation in (1b) to derive a Robin condition for the pressure-Poisson problem that takes the form

$$-p - \frac{\bar{z}_p\Delta t}{\rho}\partial_n p = \mathbf{n}^T(\bar{\boldsymbol{\sigma}}\mathbf{n} - \boldsymbol{\tau}\mathbf{n}) + \bar{z}_p\Delta t\mathbf{n}^T\big(\bar{\mathbf{v}}_t + \nu\nabla\times\nabla\times\mathbf{v}\big), \qquad \mathbf{x}\in\Gamma(t), \tag{15}$$

where $\partial_n = \mathbf{n}\cdot\nabla$ is the normal derivative and $\nu = \mu/\rho$ is the kinematic viscosity of the fluid. Following [8], we have used the identity, $\Delta\mathbf{v} = -\nabla\times\nabla\times\mathbf{v}$, noting that $\nabla\cdot\mathbf{v}=0$, to replace $\Delta\mathbf{v}$ on the right-hand side of (15) in favor of the curl-curl operator. This is done for improved stability of the fractional-step scheme. The condition in (15), along with suitable conditions for $\mathbf{x}\in\partial\Omega(t)\backslash\Gamma(t)$, is used for the Poisson equation in (4) for the pressure.

The AMP algorithm requires an additional *interface projection* to ensure the fluid and solid interface values match at the end of the time-step. This projection defines common interface values for the velocity and traction using an impedance-weighted average. Following the projections derived in [5] and also used in [2], the normal and tangential components of the velocity on the interface $\mathbf{x}\in\Gamma(t)$ are taken to be

$$\mathbf{n}^T\mathbf{v}^I = \frac{z_f}{z_f+\bar{z}_p}\mathbf{n}^T\mathbf{v} + \frac{\bar{z}_p}{z_f+\bar{z}_p}\mathbf{n}^T\bar{\mathbf{v}} + \frac{1}{z_f+\bar{z}_p}\mathbf{n}^T\big(\bar{\boldsymbol{\sigma}}\mathbf{n} - \boldsymbol{\sigma}\mathbf{n}\big), \tag{16a}$$

$$\mathbf{t}_m^T\mathbf{v}^I = \frac{z_f}{z_f+\bar{z}_s}\mathbf{t}_m^T\mathbf{v} + \frac{\bar{z}_s}{z_f+\bar{z}_s}\mathbf{t}_m^T\bar{\mathbf{v}} + \frac{1}{z_f+\bar{z}_s}\mathbf{t}_m^T\big(\bar{\boldsymbol{\sigma}}\mathbf{n} - \boldsymbol{\sigma}\mathbf{n}\big), \quad m=1,2, \tag{16b}$$

while the traction is defined from an inverse impedance average,

$$\mathbf{n}^T\boldsymbol{\sigma}^I\mathbf{n} = \frac{z_f^{-1}}{z_f^{-1}+\bar{z}_p^{-1}}\mathbf{n}^T\boldsymbol{\sigma}\mathbf{n} + \frac{\bar{z}_p^{-1}}{z_f^{-1}+\bar{z}_p^{-1}}\mathbf{n}^T\bar{\boldsymbol{\sigma}}\mathbf{n} + \frac{1}{z_f^{-1}+\bar{z}_p^{-1}}\mathbf{n}^T\big(\bar{\mathbf{v}} - \mathbf{v}\big), \tag{17a}$$

$$\mathbf{t}_m^T\boldsymbol{\sigma}^I\mathbf{n} = \frac{z_f^{-1}}{z_f^{-1}+\bar{z}_s^{-1}}\mathbf{t}_m^T\boldsymbol{\sigma}\mathbf{n} + \frac{\bar{z}_s^{-1}}{z_f^{-1}+\bar{z}_s^{-1}}\mathbf{t}_m^T\bar{\boldsymbol{\sigma}}\mathbf{n} + \frac{1}{z_f^{-1}+\bar{z}_s^{-1}}\mathbf{t}_m^T\big(\bar{\mathbf{v}} - \mathbf{v}\big), \quad m=1,2. \tag{17b}$$

The projections in (16) and (17) are derived in [5] for the case of a compressible fluid. For the case of an incompressible flow considered here the projections are postulated, and there is apparently no natural definition for the fluid impedance z_f. In our previous work [2] which considered viscous Stokes flow, we used $z_f = \rho H/\Delta t$, where H measured the height of the fluid domain, and the corresponding scheme was found to be very insensitive to the choice of H. This previous scaling was sufficient when using explicit time-stepping in the fluid. In the current paper, however, we use an IMEX scheme in the fluid where viscous effects are more important since the viscous CFL parameter $\nu\Delta t/h^2$ may become very large. In this regime, the previous choice of z_f does not result in a stable scheme. The analysis of a model problem that accounts for viscous effects performed in the companion paper [9], provides the suitable form for z_f which is a *key result* that leads to a stable scheme.

AMP Fluid Impedence. *The fluid impedance z_f accounting for both added-mass and viscous added-damping effects is chosen as*

$$z_f \stackrel{\text{def}}{=} \mathcal{C}_{\text{AM}}\left(\frac{\rho h}{\Delta t}\right) + \mathcal{C}_{\text{AD}}\left(\frac{\mu}{h}\right), \tag{18}$$

where ρ is the fluid density, $h = h(\mathbf{x})$ measures the fluid grid spacing in the normal direction to the interface, Δt is the time-step, μ is the dynamic viscosity of the fluid, and $\mathcal{C}_{\text{AM}} = 1$ and $\mathcal{C}_{\text{AD}} = 2$ are constants following the analysis in [9].

In agreement with [9], the choice (18) is found to yield a stable AMP algorithm for all FSI problems considered, including those covering a wide range of solid densities from very heavy to light. On the other hand, stable AMP algorithms also result when scaling the constants $\mathcal{C}_{\text{AD}}$ and $\mathcal{C}_{\text{AM}}$ by a factor of 1/2 or 2. This indicates that there is some robustness in the choice of the constants in (18). However, it appears to be important to keep both terms in (18), since failing to do so can lead to subtle instabilities at late times.

We note that with appropriate scales for length and time from the analysis in [9] given by h and Δt, respectively, there is a simple scaling argument leading to the form for z_f in (18). Consider a dimensional analysis of the fluid momentum equation in one dimension,

$$\rho v_t + p_x = \mu v_{xx}. \tag{19}$$

Let V and P be additional reference scales for velocity and pressure (stress), respectively. In the inertia-dominated limit, the two terms on the left-hand side of (19) set the scale for pressure leading to the balance

$$P = \left(\frac{\rho h}{\Delta t}\right) V.$$

The implied impedance, $(z_f)_{\text{AM}} = \rho h/\Delta t$, is expected to be dominant for added-mass effects. In the viscous-dominated limit when added-damping effects are important, the pressure gradient term in (19) balances the viscous stress term leading to

$$P = \left(\frac{\mu}{h}\right) V.$$

This balance suggests a second expression for the fluid impedance given by $(z_f)_{\text{AD}} = \mu/h$. A linear combination of the limiting forms agrees with the choice for z_f in (18).

The impedance-weighted averages (16) and (17) are defined to ensure that the interface conditions behave correctly in the limits of a heavy and light solids. In the limit of a heavy solid,

i.e. $\bar{\rho} \to \infty$ ($\bar{z}_p$, $\bar{z}_s \to \infty$), the interface conditions for the fluid should approach those of a (moving) no-slip wall. For $\bar{z}_s \to \infty$, (14b) reduces to

$$\mathbf{t}_m^T \mathbf{v} = \mathbf{t}_m^T \bar{\mathbf{v}}, \quad m = 1, 2, \qquad \mathbf{x} \in \Gamma(t), \tag{20}$$

so that the tangential components of the fluid velocity match those of the solid wall. We note that the tangential components of the interface velocity defined in (16b) agree with those given in (20) in this limit. The normal component of the fluid is given by the normal component of the interface velocity, defined in (16a), which becomes

$$\mathbf{n}^T \mathbf{v} = \mathbf{n}^T \mathbf{v}^I = \mathbf{n}^T \bar{\mathbf{v}}, \qquad \mathbf{x} \in \Gamma(t),$$

so that the normal component of the velocity of the fluid also matches that of the solid wall. In this heavy-solid limit, the divergence-free constraint applied on the boundary becomes a compatibility condition used to specify values of the normal component of the fluid velocity at ghost points. The Robin condition for the pressure given in (15) in the limit $\bar{z}_p \to \infty$ reduces to

$$-\frac{1}{\rho}\partial_n p = \mathbf{n}^T \bar{\mathbf{v}}_t + \nu \mathbf{n}^T \big(\nabla \times \nabla \times \mathbf{v}\big), \qquad \mathbf{x} \in \Gamma(t). \tag{21}$$

This Neumann condition for the pressure is often used for the pressure-Poisson problem at a no-slip wall.

In the limit of a light solid, i.e. $\bar{\rho} \to 0$ ($\bar{z}_p$, $\bar{z}_s \to 0$), the interface conditions for the fluid should approach those of a free surface. With $\bar{z}_s \to 0$, (14b) becomes

$$\mathbf{t}_m^T \boldsymbol{\sigma} \mathbf{n} = \mathbf{t}_m^T \bar{\boldsymbol{\sigma}} \mathbf{n}, \quad m = 1, 2, \qquad \mathbf{x} \in \Gamma(t), \tag{22}$$

and thus the tangential components of the fluid stress match those of the light solid. In this limit, the conditions in (22) and the divergence-free constraint on the fluid velocity provide the boundary conditions needed to advance the velocity using (1b), along with suitable boundary conditions for $\mathbf{x} \in \partial\Omega(t) \backslash \Gamma(t)$ which we do not discuss. The interface condition in (14a) or the derived Robin condition in (15) both reduce to

$$-p = -\mathbf{n}^T \boldsymbol{\tau} \mathbf{n} + \mathbf{n}^T \bar{\boldsymbol{\sigma}} \mathbf{n}, \qquad \mathbf{x} \in \Gamma(t), \tag{23}$$

in the limit $\bar{z}_p \to 0$, and this Dirichlet condition on pressure is used for the pressure-Poisson problem. Essentially, the solid traction sets the fluid traction along the interface in the light-solid limit, and the definitions of the interface traction in (17) only confirms this assignment. Finally, the impedance-weighted averages in (16) reduce to

$$\mathbf{v}^I = \mathbf{v}, \qquad \mathbf{x} \in \Gamma(t),$$

so that the velocity of the interface is specified by the fluid velocity, as expected, which then prescribes the velocity of the solid as a boundary condition.

3.2. Discrete partitioned algorithms

In this section, the details of the AMP algorithm are presented, along with the special cases of the TP and ATP schemes for comparison. The description of the AMP algorithm here extends the framework of the original scheme given in [2] to moving grids and deforming interfaces. A semi-implicit predictor-corrector scheme is used to solve the fluid equations following the work in [8] and extending the explicit scheme in [2], while a second-order accurate upwind scheme is used to

advance the solid equations. The evolving fluid domain is discretized on a moving overlapping grid, which is discussed in more detail in Section 4. The solid domain is discretized using a static overlapping grid in its reference configuration.

Note that the main difference between the AMP scheme detailed below and the TP and ATP schemes lies in the treatment of the interface coupling conditions, which contribute a negligible computational cost as compared to the implicit solves for the fluid velocity and pressure. Thus, the overall computational cost of the AMP scheme would be similar to other partitioned schemes that employ an IMEX-type fractional-step scheme and do not use sub-iterations.

Algorithm 1 outlines the steps for the AMP scheme. Let $\mathbf{x}_{\mathbf{i}}^n$ for $\mathbf{i} \in \Omega_h$ denote the time-dependent grid points belonging to the fluid domain (including grid points on the boundaries and the interface), and let $\dot{\mathbf{x}}_{\mathbf{i}}^n$ denote the velocity of the grid points at the n^{th} time step, t^n. The indices of grid points on the interface of the fluid grid are denoted by $\mathbf{i} \in \Gamma_h$. Similarly, let $\bar{\mathbf{x}}_{\bar{\mathbf{i}}}$ for $\bar{\mathbf{i}} \in \bar{\Omega}_h$ denote the grid points belonging to the static overlapping grid for the solid (including boundaries and the interface), while $\bar{\mathbf{i}} \in \bar{\Gamma}_h$ are the indicies associated with grid points on the interface of the solid grid. Discrete approximations for the fluid variables are given by $\mathbf{v}_{\mathbf{i}}^n \approx \mathbf{v}(\mathbf{x}_{\mathbf{i}}^n, t^n)$ and $p_{\mathbf{i}}^n \approx p(\mathbf{x}_{\mathbf{i}}^n, t^n)$, while the solid variables are given by $\bar{\mathbf{u}}_{\bar{\mathbf{i}}}^n \approx \bar{\mathbf{u}}(\bar{\mathbf{x}}_{\bar{\mathbf{i}}}, t^n)$, $\bar{\mathbf{v}}_{\bar{\mathbf{i}}}^n \approx \bar{\mathbf{v}}(\bar{\mathbf{x}}_{\bar{\mathbf{i}}}, t^n)$ and $\bar{\boldsymbol{\sigma}}_{\bar{\mathbf{i}}}^n \approx \bar{\boldsymbol{\sigma}}(\bar{\mathbf{x}}_{\bar{\mathbf{i}}}, t^n)$.

In the description of the algorithm, we assume that all quantities belonging to the fluid and solid are known at $t = t^n$, and the task is to advance the solution to $t^{n+1} = t^n + \Delta t$. Algorithm 1 gives a summary of all of the stages in the AMP scheme. The first five stages of the algorithm form the *predictor* step.

Stage 1 (predict solid): Predicted values for the solid displacement are obtained by integrating (5a) using the explicit Lax-Wendroff-type scheme

$$\bar{\mathbf{u}}_{\bar{\mathbf{i}}}^{(p)} = \bar{\mathbf{u}}_{\bar{\mathbf{i}}}^n + \Delta t \bar{\mathbf{v}}_{\bar{\mathbf{i}}}^n + \frac{\Delta t^2}{2\bar{\rho}} \bar{\nabla}_h \cdot \bar{\boldsymbol{\sigma}}_{\bar{\mathbf{i}}}^n, \qquad \bar{\mathbf{i}} \in \bar{\Omega}_h.$$

Predicted values for the solid velocity and stress, contained in the vector $\bar{\mathbf{q}}_{\bar{\mathbf{i}}} = (\bar{\mathbf{v}}_{\bar{\mathbf{i}}}, \bar{\boldsymbol{\sigma}}_{\bar{\mathbf{i}}})$, are obtained using a second-order accurate Godunov upwind scheme of the form

$$\frac{\bar{\mathbf{q}}_{\bar{\mathbf{i}}}^{(p)} - \bar{\mathbf{q}}_{\bar{\mathbf{i}}}^n}{\Delta t} = -\sum_{m=1}^{3} \frac{1}{\Delta \bar{x}_m} \left(\bar{\mathbf{F}}^+_{m,\,\bar{\mathbf{i}}} - \bar{\mathbf{F}}^-_{m,\,\bar{\mathbf{i}}} \right), \qquad \bar{\mathbf{i}} \in \bar{\Omega}_h, \tag{24}$$

where $\bar{\mathbf{F}}^{\pm}_{m,\,\bar{\mathbf{i}}}$ represents the upwind fluxes corresponding to the $\bar{x}_m$ coordinate direction. In practice, we add a stress-relaxation term to the right-hand side of (24) following the approach in [18] so that the stress-strain relation in (6) is satisfied approximately throughout the solid domain.

Stage 2 (predict fluid grid motion): The computed solid displacement, $\bar{\mathbf{u}}_{\bar{\mathbf{i}}}^{(p)}$, is used to predict the position, $\mathbf{x}_{\mathbf{i}}^{(p)}$ for $\mathbf{i} \in \Gamma_h$, of the fluid-solid interface at t^{n+1}. The overlapping-grid generator is called to move the fluid grid to match the predicted interface position, and to determine the grid velocity $\dot{\mathbf{x}}_{\mathbf{i}}^{(p)}$.

Stage 3 (predict fluid velocity): The fluid velocity at t^{n+1} is predicted using an explicit Adams-Bashforth scheme for the convection and pressure-gradient terms and an implicit Crank-Nicholson scheme for the viscous terms. The scheme takes the form

$$\frac{\mathbf{v}_{\mathbf{i}}^{(p)} - \mathbf{v}_{\mathbf{i}}^n}{\Delta t} = \frac{1}{2} \left(3\mathbf{N}_h(\mathbf{v}_{\mathbf{i}}^n, p_{\mathbf{i}}^n) - \mathbf{N}_h(\mathbf{v}_{\mathbf{i}}^{n-1}, p_{\mathbf{i}}^{n-1}) \right) + \frac{1}{2} \left(\mathbf{L}_h(\mathbf{v}_{\mathbf{i}}^{(p)}) + \mathbf{L}_h(\mathbf{v}_{\mathbf{i}}^n) \right), \qquad \mathbf{i} \in \Omega_h \backslash \Gamma_h, \tag{25}$$

Algorithm 1 Added-mass partitioned (AMP) scheme

// Predictor steps

1. Predict solid:
$$\begin{cases} \bar{\mathbf{u}}_{\bar{\mathbf{i}}}^{(p)} = \bar{\mathbf{u}}_{\bar{\mathbf{i}}}^{n} + \Delta t \bar{\mathbf{v}}_{\bar{\mathbf{i}}}^{n} + \frac{\Delta t^2}{2\bar{\rho}} \bar{\nabla}_h \cdot \bar{\boldsymbol{\sigma}}_{\bar{\mathbf{i}}}^{n}, & \bar{\mathbf{i}} \in \bar{\Omega}_h. \\ \bar{\mathbf{q}}_{\bar{\mathbf{i}}}^{(p)} = \bar{\mathbf{q}}_{\bar{\mathbf{i}}}^{n} - \Delta t \sum_{m=1}^{3} \frac{1}{\Delta \bar{x}_m} \Big(\bar{\mathbf{F}}^{+}_{m,\,\bar{\mathbf{i}}} - \bar{\mathbf{F}}^{-}_{m,\,\bar{\mathbf{i}}} \Big), & \bar{\mathbf{i}} \in \bar{\Omega}_h, \end{cases}$$

2. Predict fluid grid: advance fluid grid to t^{n+1} using $\bar{\mathbf{u}}_{\bar{\mathbf{i}}}^{(p)}$ for $\bar{\mathbf{i}} \in \bar{\Gamma}_h$, and compute grid velocity.

3. Predict fluid velocity:
$$\begin{cases} \mathbf{v}_{\mathbf{i}}^{(p)} = \mathbf{v}_{\mathbf{i}}^{n} + \frac{\Delta t}{2}\big(3\mathbf{N}_h(\mathbf{v}_{\mathbf{i}}^{n}, p_{\mathbf{i}}^{n}) - \mathbf{N}_h(\mathbf{v}_{\mathbf{i}}^{n-1}, p_{\mathbf{i}}^{n-1})\big) + \frac{\Delta t}{2}\big(\mathbf{L}_h(\mathbf{v}_{\mathbf{i}}^{(p)}) + \mathbf{L}_h(\mathbf{v}_{\mathbf{i}}^{n})\big), & \mathbf{i} \in \Omega_h \backslash \Gamma_h, \\ \mathbf{t}_m^T \boldsymbol{\tau}_{\mathbf{i}}^{(p)} \mathbf{n} + \bar{z}_s \mathbf{t}_m^T \mathbf{v}_{\mathbf{i}}^{(p)} = \mathbf{t}_m^T \bar{\boldsymbol{\sigma}}_{\bar{\mathbf{i}}}^{(p)} \mathbf{n} + \bar{z}_s \mathbf{t}_m^T \bar{\mathbf{v}}_{\bar{\mathbf{i}}}^{(p)}, & \mathbf{i} \in \Gamma_h,\ \bar{\mathbf{i}} \in \bar{\Gamma}_h, \\ \nabla_h \cdot \mathbf{v}_{\mathbf{i}}^{(p)} = 0, & \mathbf{i} \in \Gamma_h, \\ \mathbf{n}^T \mathbf{v}_{\mathbf{i}}^{(p)} = \frac{z_f}{z_f + \bar{z}_p} \mathbf{n}^T \mathbf{V}_h^p(\mathbf{v}_{\mathbf{i}}^{(p)}) + \frac{\bar{z}_p}{z_f + \bar{z}_p} \mathbf{n}^T \bar{\mathbf{v}}_{\bar{\mathbf{i}}}^{(p)}, \quad \mathbf{t}_m^T \mathbf{v}_{\mathbf{i}}^{(p)} = \mathbf{t}_m^T \mathbf{V}_h^p(\mathbf{v}_{\mathbf{i}}^{(p)}), & \mathbf{i} \in \Gamma_h,\ \bar{\mathbf{i}} \in \bar{\Gamma}_h, \\ \text{Velocity boundary conditions on } \partial\Omega_h \backslash \Gamma_h. \end{cases}$$

4. Predict fluid pressure:
$$\begin{cases} \Delta_h p_{\mathbf{i}}^{(p)} = -\rho \nabla_h \mathbf{v}_{\mathbf{i}}^{(p)} : \big(\nabla_h \mathbf{v}_{\mathbf{i}}^{(p)}\big)^T + \alpha_{\mathbf{i}} \nabla_h \cdot \mathbf{v}_{\mathbf{i}}^{(p)}, & \mathbf{i} \in \Omega_h, \\ -p_{\mathbf{i}}^{(p)} - \frac{\bar{z}_p \Delta t}{\rho} (\mathbf{n} \cdot \nabla_h) p_{\mathbf{i}}^{(p)} = \mathbf{n}^T \big(\bar{\boldsymbol{\sigma}}_{\bar{\mathbf{i}}}^{(p)} \mathbf{n} - \boldsymbol{\tau}_{\mathbf{i}}^{(p)} \mathbf{n}\big) + \bar{z}_p \Delta t \mathbf{n}^T \big((\bar{\mathbf{v}}_t)_{\bar{\mathbf{i}}}^{(p)} + \nu \nabla_h \times \nabla_h \times \mathbf{v}_{\mathbf{i}}^{(p)}\big), & \mathbf{i} \in \Gamma_h,\ \bar{\mathbf{i}} \in \bar{\Gamma}_h, \\ \text{Pressure boundary conditions on } \partial\Omega_h \backslash \Gamma_h. \end{cases}$$

5. Project solid interface:
$$\begin{cases} \mathbf{n}^T \bar{\mathbf{v}}_{\bar{\mathbf{i}}}^{I} = \frac{z_f}{z_f + \bar{z}_p} \mathbf{n}^T \mathbf{v}_{\mathbf{i}}^{(p)} + \frac{\bar{z}_p}{z_f + \bar{z}_p} \mathbf{n}^T \bar{\mathbf{v}}_{\bar{\mathbf{i}}}^{(p)} + \frac{1}{z_f + \bar{z}_p} \big(\mathbf{n}^T \bar{\boldsymbol{\sigma}}_{\bar{\mathbf{i}}}^{(p)} \mathbf{n} - \mathbf{n}^T \boldsymbol{\sigma}_{\mathbf{i}}^{(p)} \mathbf{n}\big), & \bar{\mathbf{i}} \in \bar{\Gamma}_h, \mathbf{i} \in \Gamma_h, \\ \mathbf{t}_m^T \bar{\mathbf{v}}_{\bar{\mathbf{i}}}^{I} = \frac{z_f}{z_f + \bar{z}_s} \mathbf{t}_m^T \mathbf{v}_{\mathbf{i}}^{(p)} + \frac{\bar{z}_s}{z_f + \bar{z}_s} \mathbf{t}_m^T \bar{\mathbf{v}}_{\bar{\mathbf{i}}}^{(p)} + \frac{1}{z_f + \bar{z}_s} \big(\mathbf{t}_m^T \bar{\boldsymbol{\sigma}}_{\bar{\mathbf{i}}}^{(p)} \mathbf{n} - \mathbf{t}_m^T \boldsymbol{\sigma}_{\mathbf{i}}^{(p)} \mathbf{n}\big), & \bar{\mathbf{i}} \in \bar{\Gamma}_h, \mathbf{i} \in \Gamma_h, \\ \mathbf{n}^T \bar{\boldsymbol{\sigma}}_{\bar{\mathbf{i}}}^{I} \mathbf{n} = \frac{z_f^{-1}}{z_f^{-1} + \bar{z}_p^{-1}} \mathbf{n}^T \boldsymbol{\sigma}_{\mathbf{i}}^{(p)} \mathbf{n} + \frac{\bar{z}_p^{-1}}{z_f^{-1} + \bar{z}_p^{-1}} \mathbf{n}^T \bar{\boldsymbol{\sigma}}_{\bar{\mathbf{i}}}^{(p)} \mathbf{n} + \frac{1}{z_f^{-1} + \bar{z}_p^{-1}} \big(\mathbf{n}^T \bar{\mathbf{v}}_{\bar{\mathbf{i}}}^{(p)} - \mathbf{n}^T \mathbf{v}_{\mathbf{i}}^{(p)}\big), & \bar{\mathbf{i}} \in \bar{\Gamma}_h, \mathbf{i} \in \Gamma_h. \\ \mathbf{t}_m^T \bar{\boldsymbol{\sigma}}_{\bar{\mathbf{i}}}^{I} \mathbf{n} = \frac{z_f^{-1}}{z_f^{-1} + \bar{z}_s^{-1}} \mathbf{t}_m^T \boldsymbol{\sigma}_{\mathbf{i}}^{(p)} \mathbf{n} + \frac{\bar{z}_s^{-1}}{z_f^{-1} + \bar{z}_s^{-1}} \mathbf{t}_m^T \bar{\boldsymbol{\sigma}}_{\bar{\mathbf{i}}}^{(p)} \mathbf{n} + \frac{1}{z_f^{-1} + \bar{z}_s^{-1}} \big(\mathbf{t}_m^T \bar{\mathbf{v}}_{\bar{\mathbf{i}}}^{(p)} - \mathbf{t}_m^T \mathbf{v}_{\mathbf{i}}^{(p)}\big), & \bar{\mathbf{i}} \in \bar{\Gamma}_h, \mathbf{i} \in \Gamma_h, \\ \bar{\mathbf{v}}_{\bar{\mathbf{i}}}^{(p)} \leftarrow \bar{\mathbf{v}}_{\bar{\mathbf{i}}}^{I}, \quad \bar{\boldsymbol{\sigma}}_{\bar{\mathbf{i}}}^{(p)} \mathbf{n} \leftarrow \bar{\boldsymbol{\sigma}}_{\bar{\mathbf{i}}}^{I} \mathbf{n}, & \bar{\mathbf{i}} \in \bar{\Gamma}_h, \mathbf{i} \in \Gamma_h, \\ \text{Apply solid boundary conditions and set all ghost points.} \end{cases}$$

// Corrector steps

6. Correct fluid grid: recompute grid velocity using $\bar{\mathbf{v}}_{\bar{\mathbf{i}}}^{I}$ for $\bar{\mathbf{i}} \in \bar{\Gamma}_h$.

7. Correct fluid velocity:
$$\begin{cases} \mathbf{v}_{\mathbf{i}}^{n+1} = \mathbf{v}_{\mathbf{i}}^{n} + \frac{\Delta t}{2}\big(\mathbf{N}_h(\mathbf{v}_{\mathbf{i}}^{(p)}, p_{\mathbf{i}}^{(p)}) + \mathbf{N}_h(\mathbf{v}_{\mathbf{i}}^{n}, p_{\mathbf{i}}^{n})\big) + \frac{\Delta t}{2}\big(\mathbf{L}_h(\mathbf{v}_{\mathbf{i}}^{n+1}) + \mathbf{L}_h(\mathbf{v}_{\mathbf{i}}^{n})\big), & \mathbf{i} \in \Omega_h \backslash \Gamma_h, \\ \mathbf{t}_m^T \boldsymbol{\tau}_{\mathbf{i}}^{n+1} \mathbf{n} + \bar{z}_s \mathbf{t}_m^T \mathbf{v}_{\mathbf{i}}^{n+1} = \mathbf{t}_m^T \bar{\boldsymbol{\sigma}}_{\bar{\mathbf{i}}}^{I} \mathbf{n} + \bar{z}_s \mathbf{t}_m^T \bar{\mathbf{v}}_{\bar{\mathbf{i}}}^{I}, & \mathbf{i} \in \Gamma_h,\ \bar{\mathbf{i}} \in \bar{\Gamma}_h, \\ \nabla_h \cdot \mathbf{v}_{\mathbf{i}}^{n+1} = 0, & \mathbf{i} \in \Gamma_h, \\ \mathbf{n}^T \mathbf{v}_{\mathbf{i}}^{n+1} = \frac{z_f}{z_f + \bar{z}_p} \mathbf{n}^T \mathbf{V}_h(\mathbf{v}_{\mathbf{i}}^{n+1}) + \frac{\bar{z}_p}{z_f + \bar{z}_p} \mathbf{n}^T \bar{\mathbf{v}}_{\bar{\mathbf{i}}}^{I}, \quad \mathbf{t}_m^T \mathbf{v}_{\mathbf{i}}^{n+1} = \mathbf{t}_m^T \mathbf{v}_{\mathbf{i}}^{(e)}, \quad m = 1, 2, & \mathbf{i} \in \Gamma_h,\ \bar{\mathbf{i}} \in \bar{\Gamma}_h, \\ \text{Velocity boundary conditions on } \partial\Omega_h \backslash \Gamma_h. \end{cases}$$

8. Correct fluid pressure.
$$\begin{cases} \Delta_h p_{\mathbf{i}}^{n+1} = -\rho \nabla_h \mathbf{v}_{\mathbf{i}}^{n+1} : \big(\nabla_h \mathbf{v}_{\mathbf{i}}^{n+1}\big)^T + \alpha_{\mathbf{i}} \nabla_h \cdot \mathbf{v}_{\mathbf{i}}^{n+1}, & \mathbf{i} \in \Omega_h, \\ -p_{\mathbf{i}}^{n+1} - \frac{\bar{z}_p \Delta t}{\rho} (\mathbf{n} \cdot \nabla_h) p_{\mathbf{i}}^{n+1} = \mathbf{n}^T \big(\bar{\boldsymbol{\sigma}}_{\bar{\mathbf{i}}}^{I} \mathbf{n} - \boldsymbol{\tau}_{\mathbf{i}}^{n+1} \mathbf{n}\big) + \bar{z}_p \Delta t \mathbf{n}^T \big((\bar{\mathbf{v}}_t)_{\bar{\mathbf{i}}}^{I} + \nu \nabla_h \times \nabla_h \times \mathbf{v}_{\mathbf{i}}^{n+1}\big), & \mathbf{i} \in \Gamma_h,\ \bar{\mathbf{i}} \in \bar{\Gamma}_h, \\ \text{Pressure boundary conditions on } \partial\Omega_h \backslash \Gamma_h. \end{cases}$$

9. Correct solid interface.
$$\begin{cases} \bar{\mathbf{v}}_{\bar{\mathbf{i}}}^{n+1} = \mathbf{v}_{\mathbf{i}}^{n+1}, & \bar{\mathbf{i}} \in \bar{\Gamma}_h, \mathbf{i} \in \Gamma_h, \\ \bar{\boldsymbol{\sigma}}_{\bar{\mathbf{i}}}^{n+1} \mathbf{n} = \boldsymbol{\sigma}_{\mathbf{i}}^{n+1} \mathbf{n}, & \bar{\mathbf{i}} \in \bar{\Gamma}_h, \mathbf{i} \in \Gamma_h, \\ \text{Reset ghost points corresponding to } \bar{\mathbf{i}} \in \bar{\Gamma}_h. \end{cases}$$

where $\mathbf{N}_h$ and $\mathbf{L}_h$ represent grid operators associated with the explicit and implicit terms in (25), respectively, given by

$$\mathbf{N}_h(\mathbf{v_i}, p_\mathbf{i}) = -\big((\mathbf{v_i} - \dot{\mathbf{x}}_\mathbf{i}) \cdot \nabla_h\big)\mathbf{v_i} - \frac{1}{\rho}\nabla_h p_\mathbf{i}, \qquad \mathbf{L}_h(\mathbf{v_i}) = \nu\Delta_h \mathbf{v_i}. \tag{26}$$

Since $\mathbf{v}_\mathbf{i}^{(p)}$ is determined implicitly in (25), boundary conditions are required for $\mathbf{i} \in \partial\Omega_h$. Standard conditions are used for the portion of the boundary away from the interface, while care must be used in the application of the AMP interface conditions for the velocity as described in Section 3.1 so that the correct limiting behaviors are obtained. On the interface, the characteristic condition in (14b) and the divergence-free constraint give

$$\mathbf{t}_m^T\boldsymbol{\tau}_\mathbf{i}^{(p)}\mathbf{n} + \bar{z}_s\mathbf{t}_m^T\mathbf{v}_\mathbf{i}^{(p)} = \mathbf{t}_m^T\bar{\boldsymbol{\sigma}}_{\bar{\mathbf{i}}}^{(p)}\mathbf{n} + \bar{z}_s\mathbf{t}_m^T\bar{\mathbf{v}}_{\bar{\mathbf{i}}}^{(p)}, \qquad m = 1, 2, \qquad \mathbf{i} \in \Gamma_h,\ \bar{\mathbf{i}} \in \bar{\Gamma}_h, \tag{27a}$$

$$\nabla_h \cdot \mathbf{v}_\mathbf{i}^{(p)} = 0, \qquad \mathbf{i} \in \Gamma_h, \tag{27b}$$

where the interface normal, $\mathbf{n}$, and tangent vectors, $\mathbf{t}_m$, are evaluated at grids points $\mathbf{i} \in \Gamma_h$ along the predicted interface at t^{n+1}. Since (25) excludes the grids points on the interface, another set of equations are required to complete the system for the implicit time step. We use the following impedance-weighted averages to set the velocity on the interface:

$$\mathbf{n}^T\mathbf{v}_\mathbf{i}^{(p)} = \frac{z_f}{z_f + \bar{z}_p}\mathbf{n}^T\mathbf{V}_h^p(\mathbf{v}_\mathbf{i}^{(p)}) + \frac{\bar{z}_p}{z_f + \bar{z}_p}\mathbf{n}^T\bar{\mathbf{v}}_{\bar{\mathbf{i}}}^{(p)}, \qquad \mathbf{i} \in \Gamma_h,\ \bar{\mathbf{i}} \in \bar{\Gamma}_h, \tag{28a}$$

$$\mathbf{t}_m^T\mathbf{v}_\mathbf{i}^{(p)} = \mathbf{t}_m^T\mathbf{V}_h^p(\mathbf{v}_\mathbf{i}^{(p)}), \qquad m = 1, 2, \qquad \mathbf{i} \in \Gamma_h,\ \bar{\mathbf{i}} \in \bar{\Gamma}_h, \tag{28b}$$

where $\mathbf{V}_h^p$ is defined by

$$\mathbf{V}_h^p(\mathbf{v}_\mathbf{i}^{(p)}) \stackrel{\text{def}}{=} \mathbf{v}_\mathbf{i}^n + \frac{\Delta t}{2}\left(3\mathbf{N}_h(\mathbf{v}_\mathbf{i}^n, p_\mathbf{i}^n) - \mathbf{N}_h(\mathbf{v}_\mathbf{i}^{n-1}, p_\mathbf{i}^{n-1})\right) + \frac{\Delta t}{2}\Big(\mathbf{L}_h(\mathbf{v}_\mathbf{i}^{(p)}) + \mathbf{L}_h(\mathbf{v}_\mathbf{i}^n)\Big). \tag{29}$$

Equation (28a) comes from (16a) but neglecting the jump in stress terms since we do not have a good approximation to the stresses at this stage; this term is formally zero if the tractions match and is not essential to either the accuracy or stability of the algorithm. Note that (28), with $\mathbf{V}_h^p$ in (29), forms a set of equations for $\mathbf{v}_\mathbf{i}^{(p)}$, $\mathbf{i} \in \Gamma_h$, which couples to the evolution equations in (25) and the boundary conditions in (27). Together, this linear system is solved to obtain the predicted fluid velocity $\mathbf{v}_\mathbf{i}^{(p)}$.

The TP scheme sets the fluid velocity on the interface to equal that of the solid, so that the interface conditions in (28) are replaced by

$$\mathbf{v}_\mathbf{i}^{(p)} = \bar{\mathbf{v}}_{\bar{\mathbf{i}}}^{(p)}, \quad \mathbf{i} \in \Gamma_h,\ \bar{\mathbf{i}} \in \bar{\Gamma}_h.$$

The divergence-free constraint in (27b) is used to specify the normal component of the fluid velocity in the ghost points, while the tangential components of the velocity in the ghost points are extrapolated. The ATP scheme, on the other hand, applies a tangential stress boundary condition on the fluid along with the divergence-free constraint. These conditions are equivalent to the conditions in (27), but with the terms in (27a) involving the fluid and solid velocity dropped (effectively setting $\bar{z}_s = 0$), and then replacing the interface conditions in (28) with $\mathbf{v}_\mathbf{i}^{(p)} = \mathbf{V}_h^p(\mathbf{v}_\mathbf{i}^{(p)})$ for $\mathbf{i} \in \Gamma_h$. We note that these limiting cases for TP and ATP schemes correspond to the limits of the continuous conditions discussed above in Section 3.1.

Stage 4 (predict fluid pressure): Predicted values for the fluid pressure are obtained by solving the discrete Poisson problem

$$\Delta_h p_{\mathbf{i}}^{(p)} = -\rho \nabla_h \mathbf{v}_{\mathbf{i}}^{(p)} : \left(\nabla_h \mathbf{v}_{\mathbf{i}}^{(p)}\right)^T + \alpha_{\mathbf{i}} \nabla_h \cdot \mathbf{v}_{\mathbf{i}}^{(p)}, \qquad \mathbf{i} \in \Omega_h, \tag{30}$$

with the predicted fluid velocity from the previous stage used to determine the right-hand side of (30). We have included a *divergence damping* term to the right-hand side of (30) with coefficient $\alpha_{\mathbf{i}}$ to suppress the growth of the divergence of the velocity in the numerical solution that may occur due to discretization errors. The discrete approximation of the Robin condition in (15) is

$$\begin{aligned} -p_{\mathbf{i}}^{(p)} - \frac{\bar{z}_p \Delta t}{\rho}(\mathbf{n}\cdot\nabla_h) p_{\mathbf{i}}^{(p)} &= \mathbf{n}^T \left(\bar{\boldsymbol{\sigma}}_{\bar{\mathbf{i}}}^{(p)}\mathbf{n} - \boldsymbol{\tau}_{\mathbf{i}}^{(p)}\mathbf{n}\right) \\ &\quad + \bar{z}_p \Delta t \mathbf{n}^T \left((\bar{\mathbf{v}}_t)_{\bar{\mathbf{i}}}^{(p)} + \nu \nabla_h \times \nabla_h \times \mathbf{v}_{\mathbf{i}}^{(p)}\right), \qquad \mathbf{i} \in \Gamma_h,\ \bar{\mathbf{i}} \in \bar{\Gamma}_h, \end{aligned} \tag{31}$$

In the TP scheme, the Robin condition in (31) is replaced by a discrete approximation of (21) given by

$$-\frac{1}{\rho}(\mathbf{n}\cdot\nabla_h) p_{\mathbf{i}}^{(p)} = \bar{\mathbf{n}}^T \left((\bar{\mathbf{v}}_t)_{\bar{\mathbf{i}}}^{(p)} + \nu \nabla_h \times \nabla_h \times \mathbf{v}_{\mathbf{i}}^{(p)}\right), \qquad \mathbf{i} \in \Gamma_h,\ \bar{\mathbf{i}} \in \bar{\Gamma}_h,$$

whereas the ATP scheme uses an approximation of (23) given by

$$-p_{\mathbf{i}}^{(p)} = \mathbf{n}^T \left(\bar{\boldsymbol{\sigma}}_{\bar{\mathbf{i}}}^{(p)}\mathbf{n} - \boldsymbol{\tau}_{\mathbf{i}}^{(p)}\mathbf{n}\right), \qquad \mathbf{i} \in \Gamma_h,\ \bar{\mathbf{i}} \in \bar{\Gamma}_h.$$

As before, the both cases are consistent with the limiting cases of a heavy (TP) and light (ATP) solid.

Stage 5 (predict solid interface): The projections given by (16) and (17) are used in this stage to define values for the solid velocity and traction on the interface $\bar{\mathbf{i}} \in \bar{\Gamma}_h$ ($\mathbf{i} \in \Gamma_h$) as

$$\begin{aligned} \mathbf{n}^T \bar{\mathbf{v}}_{\bar{\mathbf{i}}}^I &= \frac{z_f}{z_f + \bar{z}_p}\mathbf{n}^T \mathbf{v}_{\mathbf{i}}^{(p)} + \frac{\bar{z}_p}{z_f + \bar{z}_p}\mathbf{n}^T \bar{\mathbf{v}}_{\bar{\mathbf{i}}}^{(p)} + \frac{1}{z_f + \bar{z}_p}\left(\mathbf{n}^T \bar{\boldsymbol{\sigma}}_{\bar{\mathbf{i}}}^{(p)}\mathbf{n} - \mathbf{n}^T \boldsymbol{\sigma}_{\mathbf{i}}^{(p)}\mathbf{n}\right), \\ \mathbf{t}_m^T \bar{\mathbf{v}}_{\bar{\mathbf{i}}}^I &= \frac{z_f}{z_f + \bar{z}_s}\mathbf{t}_m^T \mathbf{v}_{\mathbf{i}}^{(p)} + \frac{\bar{z}_s}{z_f + \bar{z}_s}\mathbf{t}_m^T \bar{\mathbf{v}}_{\bar{\mathbf{i}}}^{(p)} + \frac{1}{z_f + \bar{z}_s}\left(\mathbf{t}_m^T \bar{\boldsymbol{\sigma}}_{\bar{\mathbf{i}}}^{(p)}\mathbf{n} - \mathbf{t}_m^T \boldsymbol{\sigma}_{\mathbf{i}}^{(p)}\mathbf{n}\right), \end{aligned}$$

and

$$\begin{aligned} \mathbf{n}^T \bar{\boldsymbol{\sigma}}_{\bar{\mathbf{i}}}^I \mathbf{n} &= \frac{z_f^{-1}}{z_f^{-1} + \bar{z}_p^{-1}}\mathbf{n}^T \boldsymbol{\sigma}_{\mathbf{i}}^{(p)}\mathbf{n} + \frac{\bar{z}_p^{-1}}{z_f^{-1} + \bar{z}_p^{-1}}\mathbf{n}^T \bar{\boldsymbol{\sigma}}_{\bar{\mathbf{i}}}^{(p)}\mathbf{n} + \frac{1}{z_f^{-1} + \bar{z}_p^{-1}}\left(\mathbf{n}^T \bar{\mathbf{v}}_{\bar{\mathbf{i}}}^{(p)} - \mathbf{n}^T \mathbf{v}_{\mathbf{i}}^{(p)}\right), \\ \mathbf{t}_m^T \bar{\boldsymbol{\sigma}}_{\bar{\mathbf{i}}}^I \mathbf{n} &= \frac{z_f^{-1}}{z_f^{-1} + \bar{z}_s^{-1}}\mathbf{t}_m^T \boldsymbol{\sigma}_{\mathbf{i}}^{(p)}\mathbf{n} + \frac{\bar{z}_s^{-1}}{z_f^{-1} + \bar{z}_s^{-1}}\mathbf{t}_m^T \bar{\boldsymbol{\sigma}}_{\bar{\mathbf{i}}}^{(p)}\mathbf{n} + \frac{1}{z_f^{-1} + \bar{z}_s^{-1}}\left(\mathbf{t}_m^T \bar{\mathbf{v}}_{\bar{\mathbf{i}}}^{(p)} - \mathbf{t}_m^T \mathbf{v}_{\mathbf{i}}^{(p)}\right), \end{aligned}$$

respectively. These projected values are used to specify $\bar{\mathbf{v}}_{\bar{\mathbf{i}}}^{(p)}$ and $\bar{\boldsymbol{\sigma}}_{\bar{\mathbf{i}}}^{(p)}\mathbf{n}$ on the interface, and then the corresponding values in the ghost points are set using extrapolation.

In the TP scheme, we use $\bar{\boldsymbol{\sigma}}_{\bar{\mathbf{i}}}^{(p)}\mathbf{n} = \boldsymbol{\sigma}_{\mathbf{i}}^{(p)}\mathbf{n}$ to set the predicted solid traction on the interface, but then use the compatibility condition

$$\bar{\lambda}\left(\bar{\nabla}_h \cdot \bar{\mathbf{v}}_{\bar{\mathbf{i}}}^{(p)}\right)\bar{\mathbf{n}} + \bar{\mu}\left(\bar{\nabla}_h \bar{\mathbf{v}}_{\bar{\mathbf{i}}}^{(p)} + \left(\bar{\nabla}_h \bar{\mathbf{v}}_{\bar{\mathbf{i}}}^{(p)}\right)^T\right)\bar{\mathbf{n}} = \dot{\bar{\boldsymbol{\sigma}}}_{\bar{\mathbf{i}}}\bar{\mathbf{n}}, \qquad \bar{\mathbf{i}} \in \bar{\Gamma}_h, \tag{32}$$

which can be interpreted as a set of discrete Neumann conditions for the components of $\bar{\mathbf{v}}^{(p)}_{\bar{\mathbf{i}}}$. The time-derivative of the solid stress on the right-hand side of (32) is obtained using a second-order accurate approximation involving $\bar{\boldsymbol{\sigma}}^{(p)}_{\bar{\mathbf{i}}}$ and the solid stress at t^n and t^{n-1}. For the ATP scheme, we set the solid velocity on the interface using $\bar{\mathbf{v}}^{(p)}_{\bar{\mathbf{i}}} = \mathbf{v}^{(p)}_{\mathbf{i}}$, and use the compatibility condition

$$\bar{\nabla}_h \cdot \bar{\boldsymbol{\sigma}}^{(p)}_{\bar{\mathbf{i}}} = \rho \dot{\bar{\mathbf{v}}}^{(p)}_{\bar{\mathbf{i}}}, \qquad \bar{\mathbf{i}} \in \bar{\Gamma}_h,$$

which can be interpreted as a set of discrete Neumann conditions for the components of $\bar{\boldsymbol{\sigma}}^{(p)}_{\bar{\mathbf{i}}}\mathbf{n}$. The acceleration of the solid on the interface is computed using a finite-difference approximation similar to that described to compute the stress for the TP scheme.

This completes the set of stages used for the predictor step of Algorithm 1. The remaining four stages form the *corrector* step. Stages 7 and 8 in the corrector step are similar in form to the corresponding two stages in the predictor step. In Stage 9 the solid velocity and traction are set equal to the current fluid values. This ensures that the interface jump conditions are exactly matched at the end of the correction step. The boundary conditions for the TP and ATP scheme in the corrector stages are handled in an analogous fashion to the predictor stages.

4. Spatial approximations

The domain for the FSI problem is discretized using an overlapping grid $\mathcal{G}$, which is defined by a set of component grids $\{G_g\}$, $g = 1, \ldots, \mathcal{N}$, that cover both the fluid and solid domains. Static Cartesian background grids are used for the bulk of each domain, while boundary and interface-fitted grids are used to resolve curved boundaries and moving fluid-solid interfaces (see Figure 2). In the fluid, each component grid is defined by a mapping from the physical space $\mathbf{x}$ to a unit computational space $\mathbf{r}$ (a square in two dimensions or a box in three dimensions). The mapping is time dependent in general to account for the moving fluid-solid interface, and is given by

$$\mathbf{x} = \mathbf{G}_g(\mathbf{r}, t), \qquad \mathbf{r} \in [0,1]^{n_d}, \quad \mathbf{x} \in \mathbb{R}^{n_d},$$

where n_d is the number of dimensions. Each component grid for the solid is defined by a mapping from the (fixed) reference space $\bar{\mathbf{x}}$ to a unit computational space, and is given by

$$\bar{\mathbf{x}} = \bar{\mathbf{G}}_g(\mathbf{r}), \qquad \mathbf{r} \in [0,1]^{n_d}, \quad \bar{\mathbf{x}} \in \mathbb{R}^{n_d}.$$

The corresponding physical space $\mathbf{x}$ for the solid is then determined by the mapping in (7) using the computed displacement $\bar{\mathbf{u}}(\bar{\mathbf{x}}, t)$.

The grid points on a component grid are marked as discretization points (where the governing equations or boundary conditions are discretized), unused points (points that are not used in the discretization) and interpolation points, as indicated in Figure 2. Solution values at interpolation points are generally determined from a tensor-product Lagrange interpolant in the parameter space of the donor grid. Ghost points are used to facilitate the discretization of boundary conditions. The classification of grid points into discretization, interpolation and unused points (*grid connectivity*) is determined by an overlapping grid generator. We use the `Ogen` grid generator [46]. `Ogen` takes as input a set of overlapping component grids (for one or more domains) along with a classification of the boundaries of each grid as a physical boundary (including the interface between fluid and solid domains), an interpolation boundary or a periodic boundary. Unused points are determined by `Ogen` using physical boundaries to mark points exterior to the domain following a *hole-cutting* algorithm. The remaining points are classified as either discretization points or interpolation points.

The position of the fluid-solid interface is defined from the computed solid displacement using $\mathbf{x} = \bar{\mathbf{x}} + \bar{\mathbf{u}}(\bar{\mathbf{x}}, t)$ on the interface, and this defines the boundary of the adjacent fluid grid. A hyperbolic grid generator [47] is used to generate the fluid grid near the interface by marching from the interface a short distance into the fluid domain. `Ogen` is called to regenerate the overlapping grid connectivity between the (moving) interface-fitted grids of the fluid and the (static) background grids. Note that some points on the component grids change from active points (i.e. discretization or interpolation points) to unused points as the mesh deforms. Special treatment is required for the reverse situation in which unused point become active points. These *exposed* points require suitable solution values at past times, see [6] for further details. In the implementation of the AMP scheme, all points (active and unused) are kept in the matrix for any linear system solve, while the equations for each point depend on whether it is active or not. If, for example, a point is an active interpolation point, then the weights in the interpolation formula are included in the matrix.

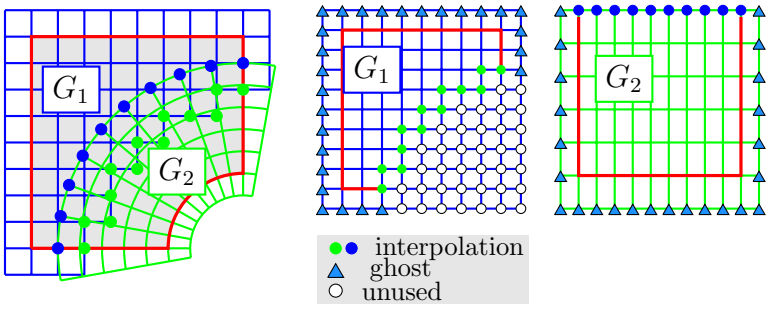

Figure 2: Left: composite of a background grid (G_1, blue) and a boundary-fitted grid (G_2, green) in physical space for the domain defined by the interior of the red boundary. The grid points on G_1 with green dots interpolate from G_2 and the grid points on G_2 with blue dots interpolate from G_1. Middle: Plot of G_1 showing interpolation points, ghost points (grid points which exist outside the physical boundary), and unused points (grid points which do not affect the computation). Right: The green boundary fitted grid, G_2, is mapped to a unit square. The plot shows interpolation points and ghost points.

The Navier-Stokes equations for the fluid in velocity-pressure form are transformed to the unit-square coordinates, $\mathbf{r}$, using standard chain-rule differentiation formulas. On moving grids, the equations are transformed to a moving coordinate system which introduces the grid velocity, $\dot{\mathbf{x}}$, into the advection terms as indicated in (25) and (26). The resulting equations are then discretized using standard finite-difference approximations for the derivatives with respect to $\mathbf{r}$ following the approach in [6, 8, 48]. The equations of linear elasticity for the solid are also transformed to the unit-square coordinates and then integrated in time using a (Godunov-based) upwind scheme similar to [5, 7, 18]. The approximations of the equations governing the fluid and solid are second-order accurate in the present implementation of the AMP time-stepping scheme.

The time step, Δt, is taken as the minimum value between the stable time steps for the fluid and solid domain solvers independently. There is no restriction on the time step imposed by the AMP interface conditions. For the fluid solver, the time step is generally determined by a CFL-type stability constraint based on the advection terms in the fluid momentum equations. The viscous terms are integrated implicitly so that there is no stability constraint on Δt arising from these terms. The time step for the solid solver is determined based on a CFL-type stability constraint involving the compression wave speed, but there also may be an adjustment imposed by the stress-relaxation term (see [7, 18]).

5. Numerical results

We now present numerical results to verify the stability and accuracy of the AMP scheme for a variety of FSI problems. We begin by comparing the results of the new AMP scheme to those given by the traditional partitioned (TP) scheme (with sub-iterations) for an FSI problem involving a rectangular elastic piston. An exact solution is available for this problem, which is used to determine the convergence behavior of both methods as the grid is refined. We then consider two FSI problems involving an annular geometry for which exact solutions are found. The first problem involves an annular fluid region surrounding an elastic solid disk with the motion of the solid constrained to the radial direction normal to the fluid-solid interface. The second problem uses the same geometry, but assumes circumferential motion of the solid. Exact solutions for these problems are discussed in Appendix A and Appendix B, while the results are given in Sections 5.2.1 and 5.2.2 below. We next test the AMP scheme for a more general FSI problem involving a radial traveling wave. Results for this problem are given in Section 5.3 with the corresponding exact solution for a linearized traveling wave derived in Appendix C. For each of these test cases, we examine the convergence of the numerical solution using the exact solution for different fluid-solid density ratios to confirm that the AMP scheme is both stable and second-order accurate. The remaining two tests involve more complex FSI problems for which exact solutions are unavailable. The first problem, discussed in Section 5.4, considers a pressure-driven flow in a channel about an elastic solid. A self-convergence study is performed for this clean benchmark problem which further verifies the accuracy and stability of the AMP scheme. We also examine the behavior of the TP scheme for this problem. The final test problem involves the flow past multiple solids with a wide range of densities. This test is discussed in Section 5.5 and is designed to illustrate the robustness of the AMP scheme. Note that for the numerical results presented in this section, the grid spacing h in the formula for the fluid impedance (18) is taken to be constant over each interface with a value equal to the minimum grid spacing in the normal direction to the interface.

5.1. Rectangular elastic piston

The geometry of the rectangular elastic piston problem is shown in Figure 3. The plot on the left shows the configuration at $t = 0$. Initially, the fluid occupies the physical domain between $y = 0$ and $y = H$, while the solid lies in its reference domain between $\bar{y} = -\bar{H}$ and $\bar{y} = 0$. It is assumed that there is no dependence in the x-direction so that the fluid-solid interface remains flat at a position $y = y_I(t)$ as shown in the middle plot. In the fluid domain, $\Omega(t)$, it is assumed that the horizontal component of velocity v_1 is zero, and thus the vertical component v_2 is a function of t alone according to the continuity equation.

Solutions to this FSI problem can be constructed for a specified motion of the fluid solid interface. The solution is summarized here with [10] providing more details of its derivation. We choose an interface position $y_I(t)$ that oscillates in the vertical direction with frequency ω and an amplitude a given by

$$y_I(t) = a\sin(\omega t), \qquad a = 2\alpha\sin(\omega\bar{H}/\bar{c}_p). \tag{33}$$

The choice in (33) corresponds to the solution for the vertical displacement of the solid given by

$$\bar{u}_2(\bar{y}, t) = \bar{F}(t - (\bar{y} + \bar{H})/\bar{c}_p) - \bar{F}(t + (\bar{y} + \bar{H})/\bar{c}_p),$$

with the smooth function $F(\bar{\tau})$ taken to be

$$\bar{F}(\bar{\tau}) = \alpha\cos(\omega\bar{\tau}),$$

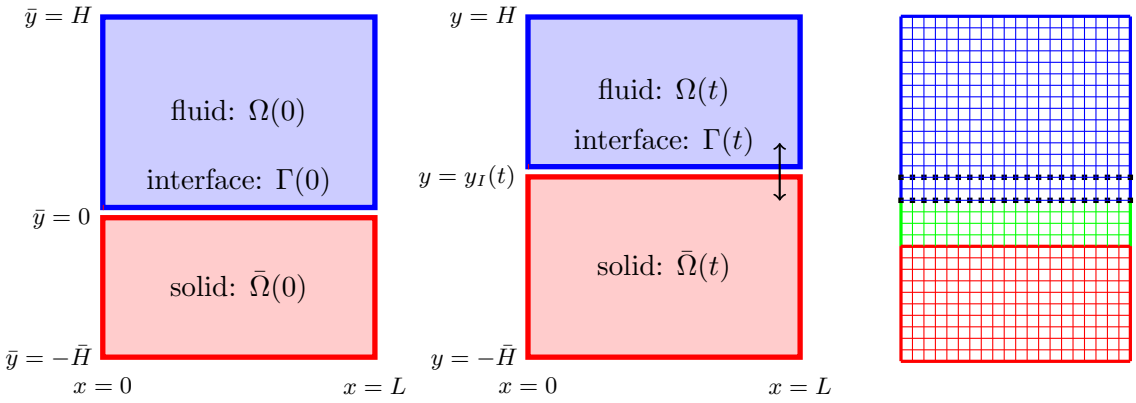

Figure 3: The geometry for the rectangular elastic piston problem. Left: initial configuration at $t = 0$. Middle: configuration for $t > 0$. Right: Composite grid $\mathbf{G}^{(2)}_{\rm rep}$ for the elastic piston. The green fluid grid adjacent to the piston moves over time. The blue fluid background grid remains fixed. The red grid for the solid reference domain also remains fixed over time.

where α is a parameter. The vertical component of the fluid velocity is $v_2(t) = y_I'(t)$, while the fluid pressure is given by

$$p(y,t) = \frac{(H-y)p_I(t) + (y - y_I(t))p_H(t)}{H - y_I(t)},$$

where

$$-p_I(t) = (\bar{\lambda} + 2\bar{\mu})\bar{u}_{2,\bar{y}}(0,t), \qquad -p_H(t) = \rho\big(H - \bar{u}_2(0,t)\big)\bar{u}_{2,tt}(0,t) + (\bar{\lambda} + 2\bar{\mu})\bar{u}_{2,\bar{y}}(0,t),$$

give the pressure at the interface and the upper boundary, $y = H$, respectively, see [10].

Numerical results are obtained using the AMP algorithm for the case $H = 1$, $\rho = 1$ and $\mu = 0.01$ for the fluid, and using $\bar{H} = 0.5$ and $\bar{\mu} = \bar{\lambda} = \bar{\rho} = \delta$ for the solid. The interface position is specified by $\alpha = 0.1$ and $\omega = \pi$. The density ratio, $\bar{\rho}/\rho = \delta$, is taken to be 10^{-3}, 1, and 10^3, representing FSI problems with very light, light and heavy solids, respectively. Numerical solutions are computed on the two-dimensional composite grid consisting of three component grids as shown in right plot of Figure 3. The composite grid, denoted by $\mathbf{G}^{(j)}_{\rm rep}$, has grid spacing equal to $h = 1/(20j)$. Boundary conditions are taken as periodic in the x-direction, consistent with the one-dimensional character of the solution. On the top fluid boundary the pressure is specified from the exact solution and the tangential component of the velocity is set to zero. The boundary conditions on the bottom solid boundary are taken as displacement conditions with the displacement and velocity specified from the exact solution. The plots in the left column of Figure 4 show the maximum-norm errors for solutions at $t_{\rm final} = 0.6$ using grid resolutions $j = 1, 2, 4, 8$. The errors in the plots indicate that AMP algorithm is converging to the exact solution at second-order accuracy.

For comparison, solutions are also computed using the TP algorithm with sub-time-step iterations. To allow for under-relaxed sub-iterations in the solid, the explicit Godunov-type upwind scheme for the solid is replaced with an upwind predictor-corrector scheme based on the improved-Euler time-stepping scheme. The TP scheme with sub-iterations thus uses a somewhat different scheme in the solid than the AMP scheme. Nevertheless the numerical errors between the two schemes are quite similar as shown below. The interface conditions in this TP scheme become strongly coupled as the sub-iterations converge, and thus upon convergence the solution serves as a surrogate for the solution of a monolithic scheme. The plots in the right column of Figure 4 show

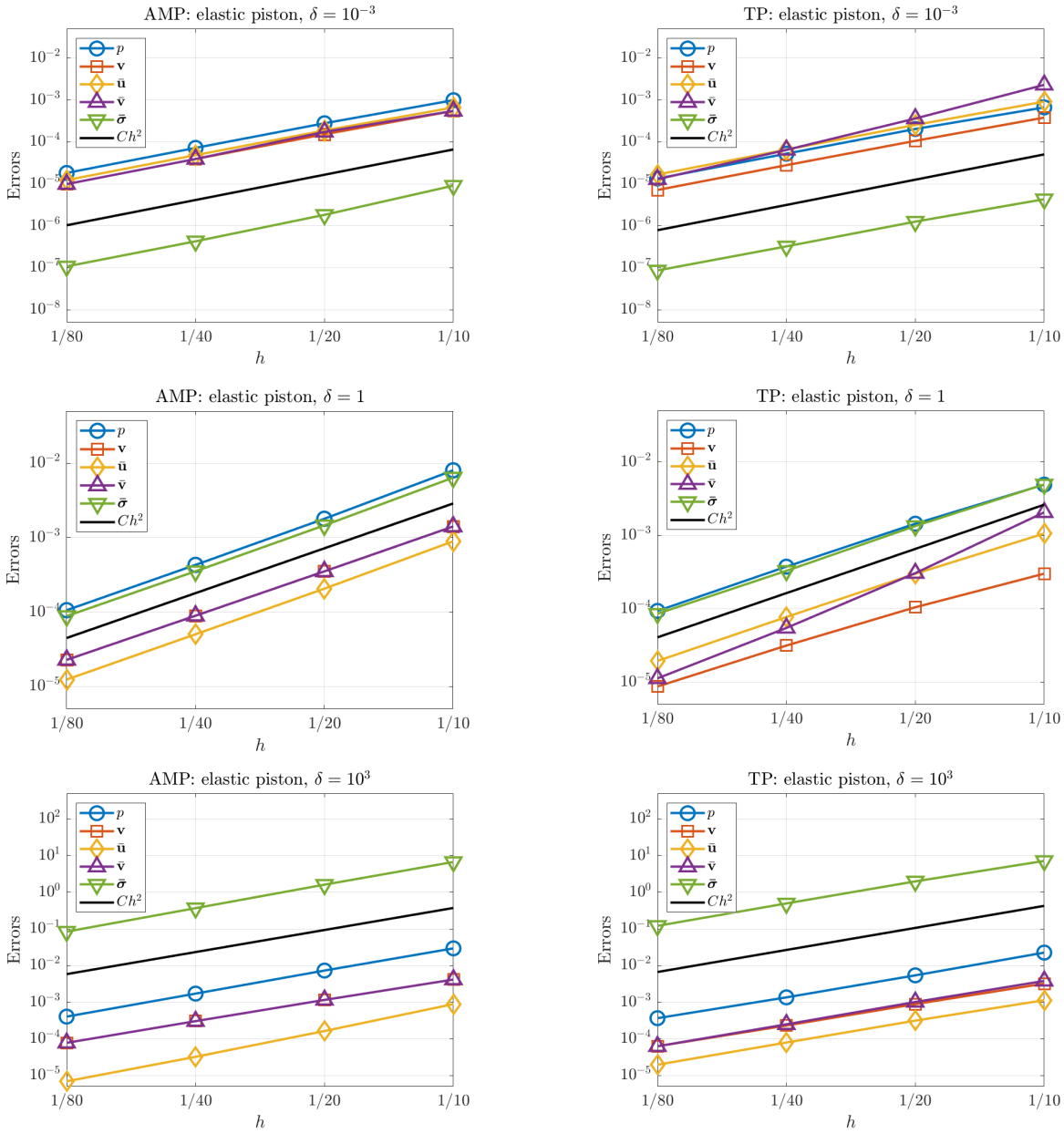

Figure 4: Grid convergence studies of the max-norm errors at time $t_{\text{final}} = 0.6$ for the block elastic piston with the AMP scheme (left) and TP scheme with sub-iterations (right). Density ratios of $\delta = 10^{-3}$ (top), $\delta = 1$ (middle), and $\delta = 10^{3}$ (bottom) are considered.

the maximum-norm errors for solutions of the rectangular elastic piston problem at $t_{\text{final}} = 0.6$. We note that the errors are nearly the same as those given by AMP algorithm (without sub-time-step iterations). In addition, the deformation of the interface as determined by the solutions of the AMP algorithm and the under-relaxed TP scheme is plotted as a function of time in Figure 5. We observe that the results of the two schemes are in very good agreement with each other, and with the curve given by the exact displacement.

A comparison of the run-time CPU performance between the AMP and TP schemes is given in Table 1. The table shows the CPU time per step and the average number of sub-iterations required per time step. For the heavy solid case of $\delta = 10^{3}$ when no sub-iterations are needed,

Table 1: Comparison of run-time performance of the AMP scheme and the TP scheme with sub-iterations for the elastic piston problem using the fine grid $\mathbf{G}^{(8)}_{\text{rep}}$ and $t_{\text{final}} = 0.6$.

Run-time performance of AMP versus TP				
δ	AMP	TP		AMP speed-up
	s/step	s/step	sub-its	TP/AMP
10^{-3}	$9.1 \cdot 10^{-2}$	2.6	310	28.8
1	$9.1 \cdot 10^{-2}$	$9.8 \cdot 10^{-1}$	111	10.7
10^{3}	$9.2 \cdot 10^{-2}$	$8.1 \cdot 10^{-2}$	0	0.9

the computational cost for the AMP and TP schemes are nearly the same. For the lighter solid cases the TP scheme with sub-iterations becomes more expensive. Note that since a sparse direct solver is being used in this relatively small-sized problem to solve the implicit equations for the fluid and pressure updates, each sub-iteration is quite fast as it only requires back-solves. We note that when using the TP scheme in practice, an acceleration procedure such as Aitken acceleration can be used to reduce the number of sub-iterations. Note, however, that the Aitken procedure is still based on accelerating an under-relaxed iteration which requires choosing the appropriate relaxation parameter, and this choice would depend on the magnitude of the added-mass and added-damping.

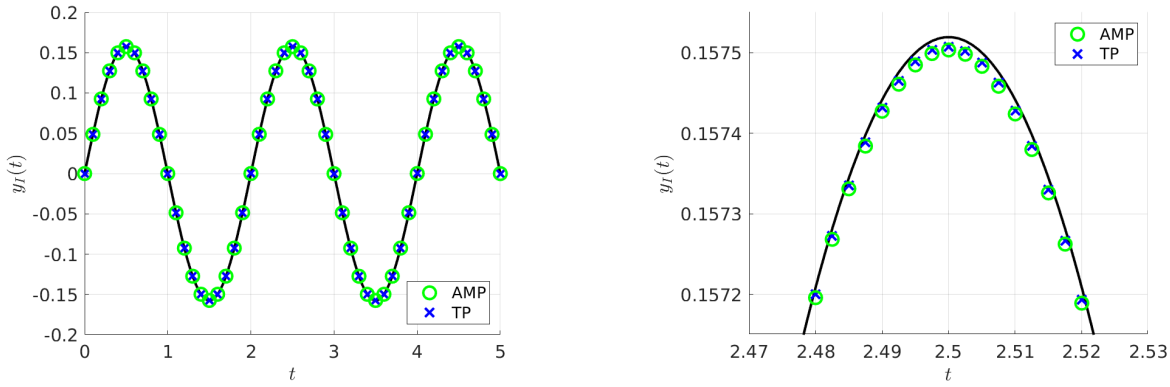

Figure 5: Comparison of interface deformation, $y_I(t)$, for the block elastic piston with density ratio $\delta = 1$ for the AMP scheme (green circles) and the TP scheme with sub-iterations (blue crosses). The exact deformation is plotted as a solid black line. The plot on the right is a close-up of the left plot near $t = 2.5$. The two schemes are seen to produce nearly the same results.

5.2. Radial elastic piston

Let us begin by considering two benchmark FSI problems for which exact solutions are available. The geometry of the two problems, shown in Figure 6, is similar. A solid elastic disk with initial radius $\bar{r} = r_I(0)$ is surrounded by an incompressible fluid which occupies the annular region $r_I(t) < r < R$. In the first problem, it is assumed that the motion of the solid and fluid is confined to the radial direction, while circumferential motion is assumed in the second problem.

5.2.1. Radial motion of a circularly symmetric elastic piston

For the case of radial motion, the solid disk behaves as an elastic piston that drives a radial flow in the fluid surrounding it (as illustrated in Figure 6). The exact solution for this problem is derived in Appendix A. It is convenient to define the solution in terms of a specified radial

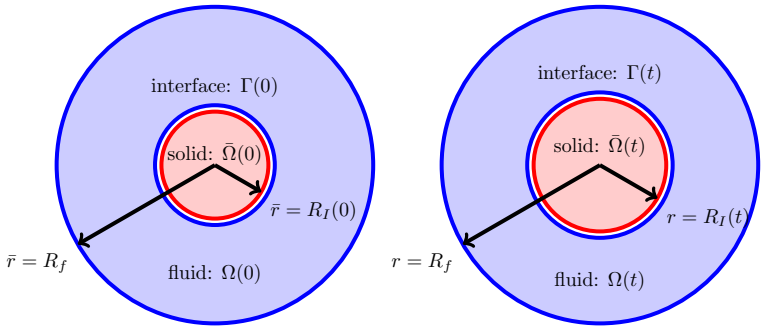

Figure 6: The geometry for the radial elastic piston solution. The left figure shows the initial domain without deformation and the right figure shows the deformed domain for $t > 0$.

component of the solid displacement, $\bar{u}_r(\bar{r}, t)$, having the form

$$\bar{u}_r(\bar{r}, t) = \beta J_1(\omega \bar{r}/\bar{c}_p) \sin(\omega t),$$

where ω is the frequency of the oscillation, β determines the amplitude, and $J_1(z)$ is the Bessel function of the first kind of order one. The corresponding time-dependent interface radius, $r_I(t)$, is given by

$$r_I(t) = r_0 + \bar{u}_r(r_0, t) = r_0 + b \sin(\omega t), \qquad b = \beta J_1(\omega r_0/\bar{c}_p), \tag{34}$$

where $r_0 = r_I(0)$ is the initial interface radius. The radial component of the fluid velocity and its pressure are given by

$$\begin{aligned} v_r(r, t) &= \frac{R}{r} V(t), \\ p(r, t) &= P(t) + \frac{\rho}{2}\left(1 - \frac{R^2}{r^2}\right) V(t)^2 + \rho R \log\left(\frac{R}{r}\right) \dot{V}(t), \end{aligned}$$

where

$$\begin{aligned} V(t) &= \frac{r_I(t)}{R} \omega \beta J_1(\omega r_0/\bar{c}_p) \cos(\omega t), \\ P(t) &= -\frac{\rho}{2}\left(1 - \frac{R^2}{r_I(t)^2}\right) V(t)^2 - \rho R \log\left(\frac{R}{r_I(t)}\right) \dot{V}(t) \\ &\quad - \beta \left[(\bar{\lambda} + 2\bar{\mu}) \frac{\omega}{\bar{c}_p} J_1'(\omega r_0/\bar{c}_p) + \frac{\bar{\lambda}}{r_0} J_1(\omega r_0/\bar{c}_p) \right] \sin(\omega t). \end{aligned}$$

Here, $V(t)$ and $P(t)$ are the radial velocity and pressure of the fluid at $r = R$, respectively, and $\dot{V}(t)$ is the radial acceleration. These functions are specified in the exact solution based on the choice for the interface motion given in (34). We take $\beta = 0.05$ to be the specified amplitude of the motion and $\omega = \pi$ as the specified frequency. Additionally, we choose $r_0 = 0.5$, $R = 1$, $\rho = 1$, and $\bar{\rho} = \bar{\mu} = \bar{\lambda} = \delta$, where δ is a parameter that determines the ratio of the density of the solid to that of the fluid.

Numerical solutions are computed using a composite grid, denoted by $\mathcal{G}_{\text{rep}}^{(j)}$, and shown in Figure 7. The grid $\mathcal{G}_{\text{rep}}^{(j)}$ has a target grid spacing of $\Delta s = 1/(10j)$ for a chosen resolution parameter j. The solid disk is represented by an inner Cartesian (red) grid and an interface-fitted annular (pink) grid. These two grids are fixed in the reference domian, $\bar{\Omega}_0$, of the solid. The fluid domain is

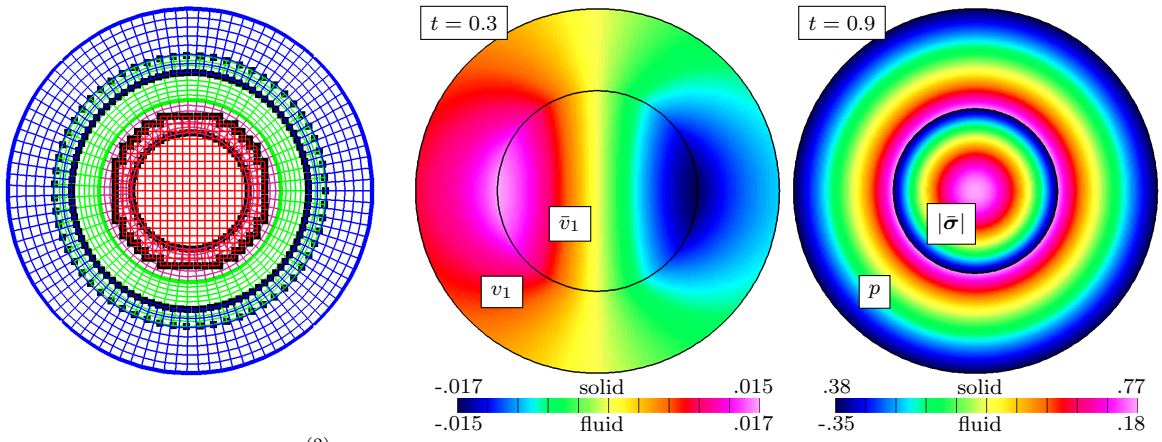

Figure 7: Left: composite grid $\mathcal{G}^{(2)}_{\text{rep}}$ for the radial elastic piston problem. The green fluid grid adjacent to the interface moves over time. The blue fluid background grid remains fixed. The red and pink grids for the solid reference domain also remain fixed over time. Middle: v_1 and $\bar{v}_1$ at $t = 0.3$. Right: p and $|\bar{\boldsymbol{\sigma}}|$ at $t = 0.9$. Solutions computed on $\mathcal{G}^{(8)}_{\text{rep}}$ with $\delta = 1$.

covered by an interface-fitted annular (green) grid that deforms over time with the radial motion of the interface, and an outer annular (blue) grid that is fixed to the outer boundary of the fluid.

Figure 7 also shows the behavior of the solution at times $t = 0.3$ and 0.9 computed using the AMP algorithm and the grid $\mathcal{G}^{(8)}_{\text{rep}}$. The density ratio for this solution is $\delta = 1$. We note that while the viscous terms in the fluid momentum equation vanish identically in the derivation of the exact solution, the numerical scheme requires a choice for the visosity which is taken to be $\nu = 0.05$. The interface between the fluid and solid expands and contracts over time. At $t = 0.3$ the interface is near its largest radius, while at $t = 0.9$ it is near its smallest.

Grid convergence studies of the max-norm errors are given in the left column of plots of Figure 8 for density ratios of $\delta = 10^3$, $\delta = 1$ and $\delta = 10^{-3}$. The computations are stable for all values of δ considered, and we observe that the max-norm errors converge at close to second-order accuracy as indicated by the (black) reference line in each plot.

5.2.2. Rotating elastic disk in a fluid annulus

The second FSI benchmark problem has a geometry similar to that shown in Figure 6, but instead of the radial motion shown we consider a circumferential motion of the disk. The exact solution, derived in Appendix B, for the circumferential components of the fluid velocity and solid displacement takes the form

$$v_\theta(r,t) = \hat{v}_\theta(r)e^{i\omega t}, \qquad \bar{u}_\theta(r,t) = \hat{\bar{u}}_\theta(r)e^{i\omega t}, \tag{35}$$

where

$$\hat{v}_\theta(r) = b\big[J_1(\lambda r)Y_1(\lambda R) - J_1(\lambda R)Y_1(\lambda r)\big], \qquad \hat{\bar{u}}_\theta(r) = \bar{b}J_1(k_s r).$$

Here,

$$b = \frac{i\omega\bar{u}_0}{J_1(\lambda r_0)Y_1(\lambda R) - J_1(\lambda R)Y_1(\lambda r_0)}, \qquad \lambda^2 = \frac{i\omega}{\nu}, \qquad \bar{b} = \frac{\bar{u}_0}{J_1(k_s r_0)}, \qquad k_s = \frac{\omega}{\bar{c}_s},$$

and $Y_1(z)$ is the Bessel function of the second kind of order one. The parameter $\bar{u}_0$ determines the amplitude of the rotational motion. Solutions for the circumferential components of the fluid velocity and the solid displacement are taken from the real parts of $v_\theta(r,t)$ and $\bar{u}_\theta(r,t)$ defined

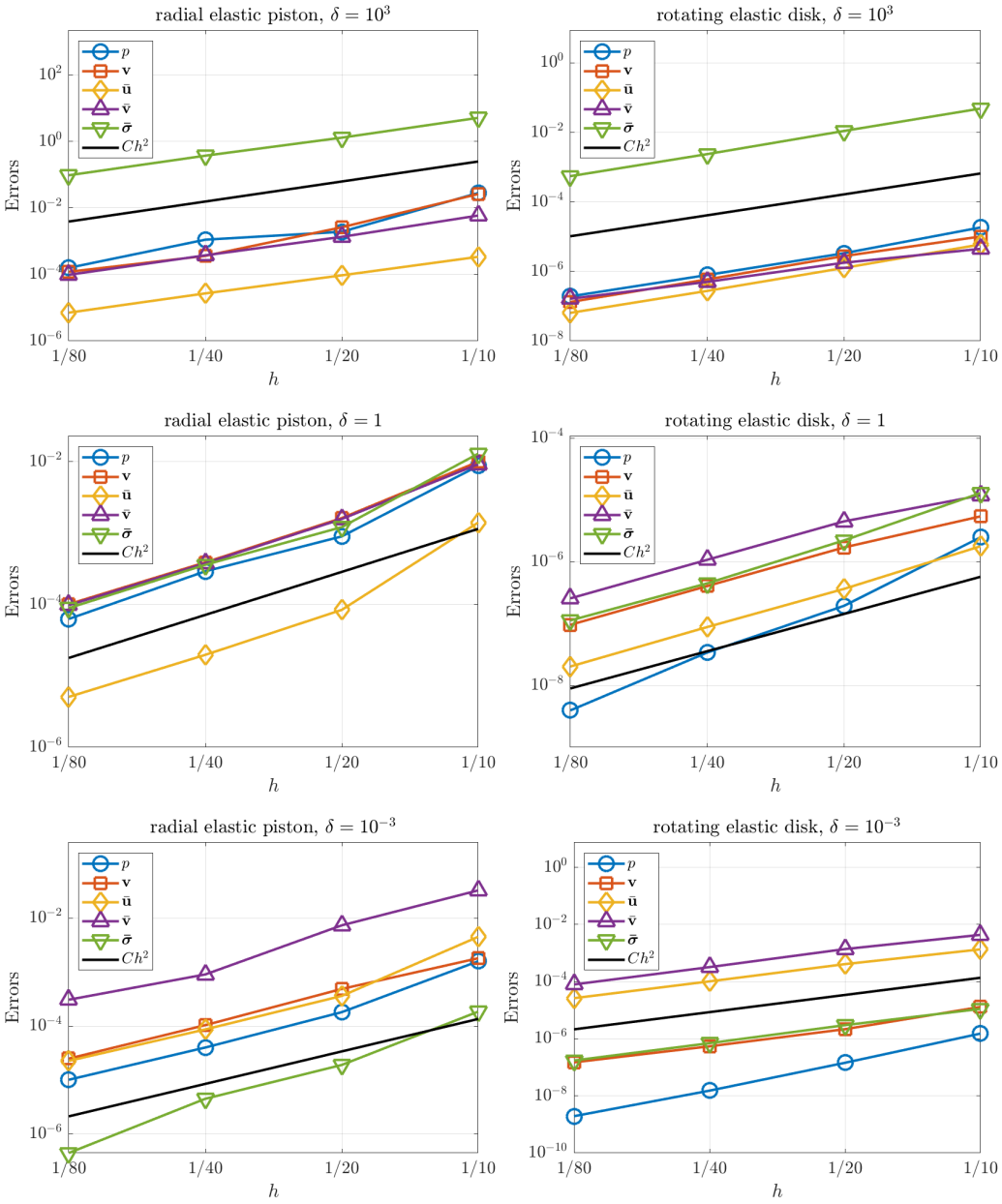

Figure 8: Grid convergence studies of the max-norm errors at time $t_f = 0.6$ for the circularly symmetric elastic piston with density ratios $\delta = 10^3$ (top left), $\delta = 1$ (middle left), and $\delta = 10^{-3}$ (bottom left) and the rotating elastic disk with density ratios $\delta = 10^3$ (top right), $\delta = 1$ (middle right), and $\delta = 10^{-3}$ (bottom right).

in (35). The pressure is then determined by

$$p(r,t) = \rho \int_{r_0}^{r} \frac{v_\theta(s,t)^2}{s}\, ds.$$

The frequency ω is obtained from the solution of the dispersion relation in (B.7). For our computations, we choose $r_0 = \frac{1}{2}$, $R = 1$, $\rho = 1$, $\nu = 0.1$, $\bar{\rho} = \bar{\mu} = \delta$ and $\bar{u}_0 = 10^{-5}$. Selected values of ω and the corresponding values for $b/\bar{u}_0$ and $\bar{b}/\bar{u}_0$ are given in Table 2 for different values of δ.

Numerical solutions are computed using the AMP algorithm and the composite grid $\mathcal{G}_{\text{rep}}^{(j)}$ as described for the previous problem. Figure 9 shows the composite grid, and the computed solution

Table 2: Selected solutions for the frequency ω of the dispersion relation in (B.7) for $\delta = 10^{-3}$, 1 and 10^3. The corresponding values for $b/\bar{u}_0$ and $\bar{b}/\bar{u}_0$ are also given. Additional parameters chosen are $r_0 = \frac{1}{2}$, $R = 1$, $\rho = 1$, $\nu = 0.1$ and $\bar{\rho} = \bar{\mu} = \delta$.

δ	ω	$b/\bar{u}_0$	$b/\bar{u}_0$
10^{-3}	$7.664 + 0.001497i$	$4.938 - 4.327i$	$-1523 + 2316i$
1	$8.778 + 0.7854i$	$4.355 - 6.155i$	$-3.512 + 1.913i$
10^3	$10.27 + 0.002055i$	$2.216 - 5.864i$	$-2.944 + 0.0005914i$

at $t = 0.1$ and 0.3 for the case $\delta = 1$. The Lamé parameter $\bar{\lambda}$ does not appear in the exact solution for this problem, but a value is required for the numerical scheme and we set $\bar{\lambda} = \delta$ in the numerical calculations.

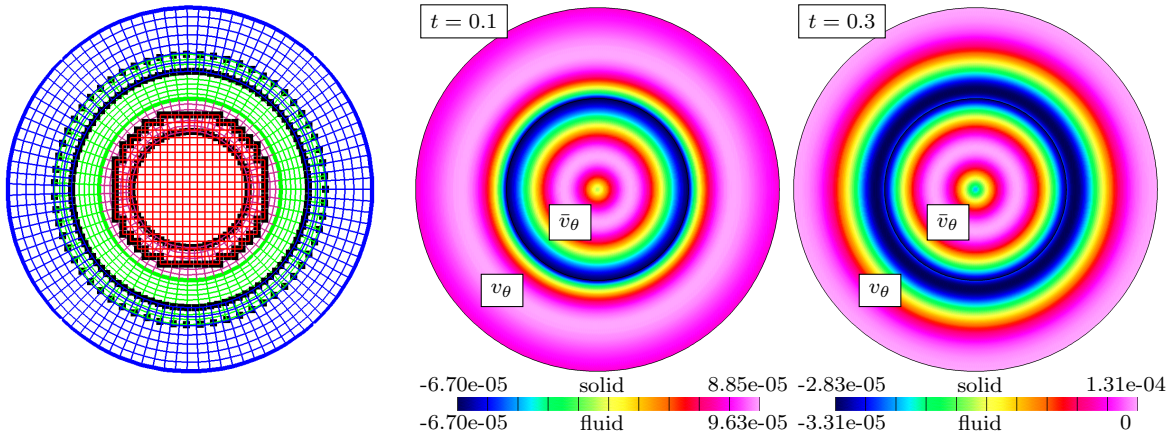

Figure 9: Left: composite grid $\mathcal{G}^{(2)}_{\text{rep}}$ for the radial elastic piston problem. The green fluid grid adjacent to the interface moves over time. The blue fluid background grid remains fixed. The red and pink grids for the solid reference domain also remain fixed over time. Middle: v_θ and $\bar{v}_\theta$ at $t = 0.1$. Right: v_θ and $\bar{v}_\theta$ at $t = 0.3$. Solutions computed on $\mathcal{G}^{(8)}_{\text{rep}}$ with $\delta = 1$.

Grid convergence studies of the max-norm errors in the right column of plots of Figure 8 for density ratios of $\delta = 10^3$, $\delta = 1$ and $\delta = 10^{-3}$. The computations are stable, as before, and the max-norm errors all converge at close to second-order accuracy.

5.3. Radial traveling wave solution

We next consider traveling wave solutions involving both radial and circumferential motion of an incompressible fluid in a circular region $0 < r < r_0$ coupled to a surrounding linearly elastic solid in the annular region $r_0 < r < R$. The geometry of the FSI problem is shown in Figure 10. An exact solution is derived for this problem in Appendix C assuming a Stokes fluid and an linearized interface about $r = r_0$. In this solution, the fluid velocity and pressure take the form

$$v_r(r,\theta,t) = \hat{v}_r(r)e^{i(n\theta-\omega t)}, \qquad v_\theta(r,\theta,t) = \hat{v}_\theta(r)e^{i(n\theta-\omega t)}, \qquad p(r,\theta,t) = \hat{p}(r)e^{i(n\theta-\omega t)},$$

where ω is a frequency, n is a positive integer, and $\hat{v}_r(r)$, $\hat{v}_\theta(r)$ and $\hat{p}(r)$ are coefficient functions. Similarly, the displacement in the solid is given by

$$\bar{u}_r(r,\theta,t) = \hat{\bar{u}}_r(r)e^{i(n\theta-\omega t)}, \qquad \bar{u}_\theta(r,\theta,t) = \hat{\bar{u}}_\theta(r)e^{i(n\theta-\omega t)},$$

with coefficient functions $\hat{\bar{u}}_r(r)$ and $\hat{\bar{u}}_\theta(r)$. Following the analysis in Appendix C, the coefficient functions are found to be

$$\hat{v}_r(r) = d\frac{J_n(\lambda r)}{r} + p_I \frac{n r^{n-1}}{\mu\lambda^2 r_0^n}, \qquad \hat{v}_\theta(r) = d\frac{i\lambda}{n} J_n'(\lambda r) + p_I \frac{i n r^{n-1}}{\mu\lambda^2 r_0^n}, \qquad \hat{p}(r) = p_I \left(\frac{r}{r_0}\right)^n,$$

and

$$\hat{\bar{u}}_r(r) = k_p \left(\bar{d}_1 J_n'(k_p r) + \bar{d}_2 Y_n'(k_p r)\right) + \frac{in}{r}\left(\bar{d}_3 J_n(k_s r) + \bar{d}_4 Y_n(k_s r)\right),$$
$$\hat{\bar{u}}_\theta(r) = -k_s \left(\bar{d}_3 J_n'(k_s r) + \bar{d}_4 Y_n'(k_s r)\right) + \frac{in}{r}\left(\bar{d}_1 J_n(k_p r) + \bar{d}_2 Y_n(k_p r)\right),$$

where $\lambda^2 = i\omega/\nu$, $k_s = \omega/\bar{c}_s$, $k_p = \omega/\bar{c}_p$, $(p_I, d, \bar{d}_1, \bar{d}_2, \bar{d}_3, \bar{d}_4)$ are constants of integration, and J_n and Y_n are Bessel functions of order n. An application of traction-free boundary conditions at $r = R$ and matching conditions involving velocity and stress at the interface $r = r_0$ leads to a homogeneous linear system of equations for the six constants. Nontrivial solutions are found if the system is singular, which leads to the dispersion relation in (C.11) involving the frequency ω and circumferential wave number n.

Numerical solutions are computed for the case $r_0 = 1$ and $R = 1.2$. The fluid has $\rho = 1$ and $\nu = 0.1$, while the solid has $\bar{\mu} = \bar{\lambda} = \bar{\rho} = \delta$. The domain for the FSI problem is represented by the composite grid, $\mathcal{G}^{(j)}_{\text{rtw}}$, with target grid spacing $\Delta s = 1/(10j)$ as shown in Figure 10. The circular fluid domain is covered by a fixed background Cartesian grid (blue) and interface-fitted grid (green). The solid domain is represented by an annular grid (red). While the exact solution assumes a linearization about a fixed interface position, $r = r_0$, the numerical solution does not make this assumption so that the interface-fitted grid of the fluid moves in time with the (very small) deformation of the interface. Also, the numerical solution does not assume a Stokes fluid. However, since the velocity of the fluid is very small for this problem, the nonlinear convective terms in the momentum equation are negligible. Initial conditions for the AMP time-stepping scheme are taken from the exact (linearized) solution at $t = 0$ for an (n, ω)-pair satisfying the dispersion relation in (C.11) and the corresponding set of constants $(p_I, d, \bar{d}_1, \bar{d}_2, \bar{d}_3, \bar{d}_4)$ with a normalization taken to be $\bar{u}_0 = 10^{-7}$. The exact solution is described in terms of complex-valued functions, but we use the real part to set the initial conditions and to compare with the numerical solution.

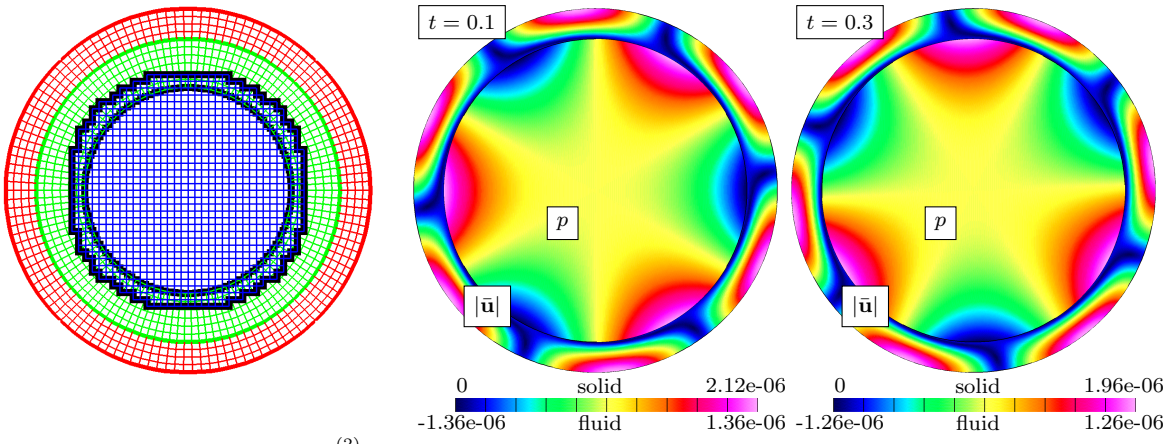

Figure 10: Left: composite grid $\mathcal{G}^{(2)}_{\text{rtw}}$ for the radial traveling wave. The green fluid grid adjacent to the interface moves over time while the blue fluid background grid remains fixed. The red grid for the solid reference domain also remains fixed over time. Middle and right: fluid pressure and $\|\bar{\mathbf{u}}\|$ at times $t = .1$ and $t = .3$, computed on grid $\mathcal{G}^{(8)}_{\text{rtw}}$ with $\delta = 1$.

Figure 10 shows representative solutions at $t = 0.1$ and 0.3 computed using the grid $\mathcal{G}^{(8)}_{\text{rtw}}$. The density ratio is chosen to be $\delta = 1$, and a (n, ω)-pair satisfying the dispersion relation is given by $n = 3$ and $\omega = 3.491 - 1.154\,i$. The shaded contours of the fluid pressure and the norm of the solid displacement both show three-fold symmetry in the circumferential direction in agreement with the choice of $n = 3$. Grid convergence studies of the max-norm errors are given in Figure 11 for density ratios of $\delta = 10$, $\delta = 1$ and $\delta = 10^{-1}$. The computations are stable and the max-norm errors all converge at close to second-order accuracy.

δ	10
ω	$4.487 - 0.1529i$
$d/\bar{u}_0$	$-0.9447 + 0.1398i$
$p_I/\bar{u}_0$	$12.41 + 13.04i$
$\bar{d}_1/\bar{u}_0$	$-1.966 - 0.1994i$
$\bar{d}_2/\bar{u}_0$	$0.3716 + 0.03041i$
$\bar{d}_3/\bar{u}_0$	$-0.01249 - 1.180i$
$\bar{d}_4/\bar{u}_0$	$-0.09547 - 0.1188i$

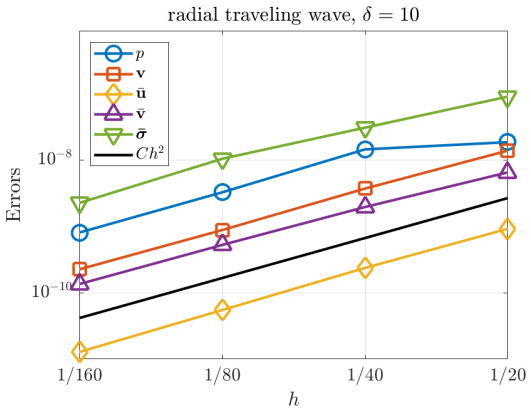

δ	1
ω	$3.491 - 1.154i$
$d/\bar{u}_0$	$-7.889 + 0.7399i$
$p_I/\bar{u}_0$	$28.98 + 23.33i$
$\bar{d}_1/\bar{u}_0$	$-5.778 - 6.619i$
$\bar{d}_2/\bar{u}_0$	$2.166 + 0.6514i$
$\bar{d}_3/\bar{u}_0$	$-0.4929 + 4.072i$
$\bar{d}_4/\bar{u}_0$	$5.728 + 2.071i$

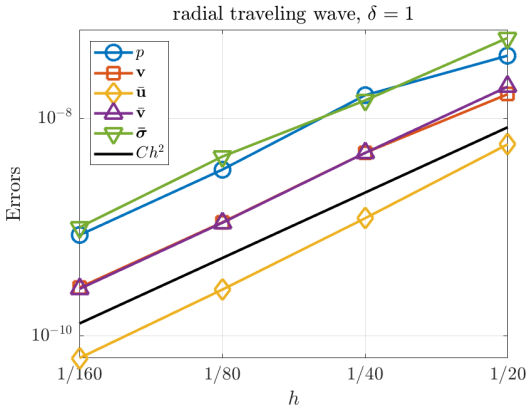

δ	10^{-1}
ω	$8.446 - 0.3587i$
$d/\bar{u}_0$	$0.08293 + 0.09885i$
$p_I/\bar{u}_0$	$-9.442 - 10.40i$
$\bar{d}_1/\bar{u}_0$	$0.4973 - 0.4251i$
$\bar{d}_2/\bar{u}_0$	$-3.942 - 2.816i$
$\bar{d}_3/\bar{u}_0$	$-5.889 + 6.165i$
$\bar{d}_4/\bar{u}_0$	$0.3925 + 5.918i$

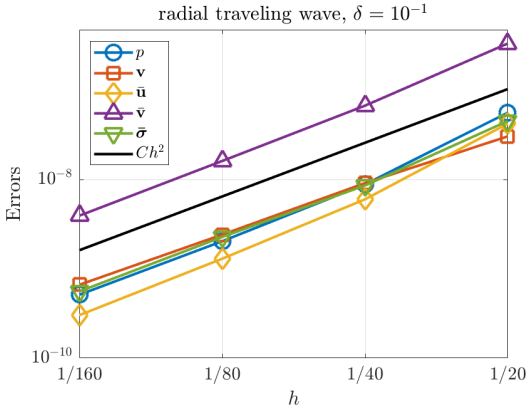

Figure 11: Grid convergence studies of the max-norm errors in the numerical solution of the radial traveling wave problem at time $t = 0.3$ for density ratios $\delta = 10$ (top right), $\delta = 1$ (middle right), and $\delta = 10^{-1}$ (bottom right). The frequencies and constants for each case are tabulated to the left of each convergence plot. For each case, $r_0 = 1$, $R = 1.2$, $\rho = 1$, $\nu = 0.1$, $\bar{\mu} = \bar{\lambda} = \bar{\rho} = \delta$ and $n = 3$.

5.4. Elastic annulus in a pressure-driven channel flow

In this section, we consider the flow of an incompressible fluid in a channel past an embedded annular elastic solid which is anchored by a fixed inner boundary. The fluid with density $\rho = 1$ and viscosity $\nu = 0.05$ exists in the rectangular region $[-3, 3] \times [-1.75, 1.75]$. The solid annulus has center $\mathbf{x} = (0, 0)$ with outer radius $R_d = 0.8$ and inner radius $R_i = 0.4$. The solid parameters are $\bar{\rho} = \bar{\lambda} = \bar{\mu} = \delta$, where the density ratio δ is a parameter defining light and heavy solids as before. Initially the fluid is at rest and the displacement of the solid is zero. A flow in the channel is driven by a pressure gradient determined by a variable pressure assigned at the inflow boundary on the left. To define a smooth solution for testing convergence, the pressure at the left inflow boundary is smoothly ramped from zero to a final value of $p_0 = 1$ at $t = 1$. Specifically, we set $p = p_0\eta(t)$ at $x = -3$, where $\eta(t)$ is a ramp function given by

$$\eta(t) = \begin{cases} (35 + (-84 + (70 - 20t)t)t)t^4, & \text{for } 0 \le t \le 1, \\ 1, & \text{for } t > 1. \end{cases} \tag{36}$$

The ramp function satisfies $\eta = \eta' = \eta'' = \eta''' = 0$ at $t = 0$, and it has three continuous derivatives at $t = 1$. We also set the tangential component of the velocity to be zero at the left inflow boundary. No-slip boundary conditions are applied at the top and bottom walls of the channel, while the pressure and normal derivatives of the velocity are set to zero at the right outflow boundary. The usual matching conditions involving velocity and stress are taken at the fluid-solid interface, and the inner solid boundary is taken as a zero displacement condition. While an exact solution is not available for this problem, the set-up is very clean so that it makes a good benchmark problem for testing various FSI algorithms as is done below.

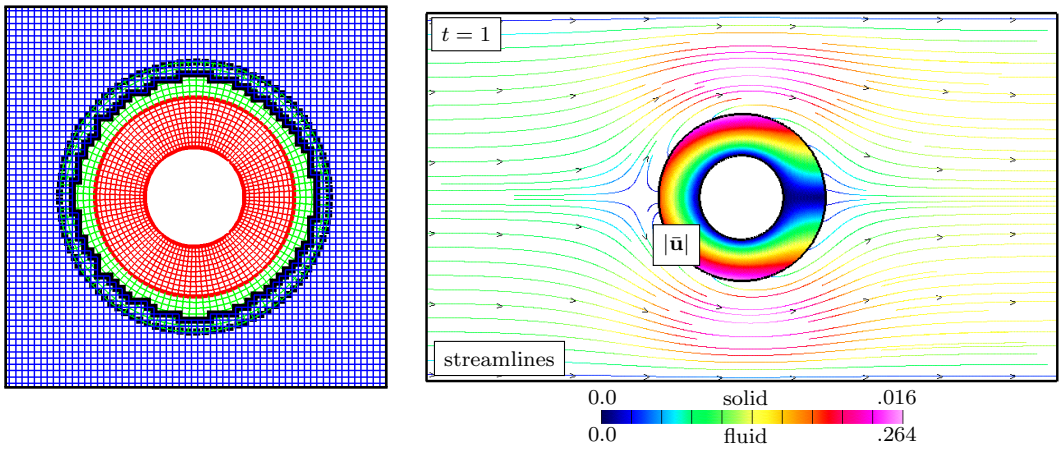

Figure 12: Left: composite grid $\mathcal{G}_d^{(2)}$ for the annulus in a channel. The green fluid grid adjacent to the interface moves over time while the blue fluid background grid remains fixed. The red grid for the solid reference domain also remains fixed over time. Right: streamlines and solid displacement norm $|\bar{\mathbf{u}}|$ for $\delta = 10$ at $t = 1.0$.

The composite grid used for this problem is denoted by $\mathcal{G}_d^{(j)}$ with target grid spacing equal to $\Delta s = 1/(10j)$. An enlarged view of the central portion of the grid is shown in Figure 12. The solid is represented by a single annular (red) grid. The fluid domain is covered by a background Cartesian (blue) grid and an annular (green) grid of radial width equal to 0.2 initially. This latter grid is attached to the interface and deforms over time.

Figures 13 and 14 describe the evolution of the fluid-solid interface over several snapshots in time. Figure 13 shows the shape of the interface in physical space at different times by indicating the displacement of a set of marker points on the interface from their reference positions at $t = 0$

to their current positions at the times given. Figure 14, on the other hand, shows the radial and circumferential components of the interface displacement as a function of the polar angle, θ, for the same set of times. The angle $\theta = 0$ corresponds to the trailing edge of the solid and θ increases in the counter-clockwise direction. At time $t = 0$ the interface is circular. The pressure at the inflow boundary ramps up from $p = 0$ at $t = 0$ to $p = 1$ at $t = 1$, and by $t = 2$ the interface has deformed with the left side being pushed to the right. Following the initial deformation of the solid to the right by the drag of the fluid, the solid undergoes elastic oscillations in time about this initially deformed shape. The oscillations in the solid are damped over time due to energy transfer to the fluid and the viscous dissipation that occurs there. We observe that the outer boundary of the solid achieves its maximum circumferential displacement (in magnitude) at approximately $\theta = 90°$ and $\theta = 270°$, while its maximum radial displacement occurs at the leading edge $\theta = 180°$.

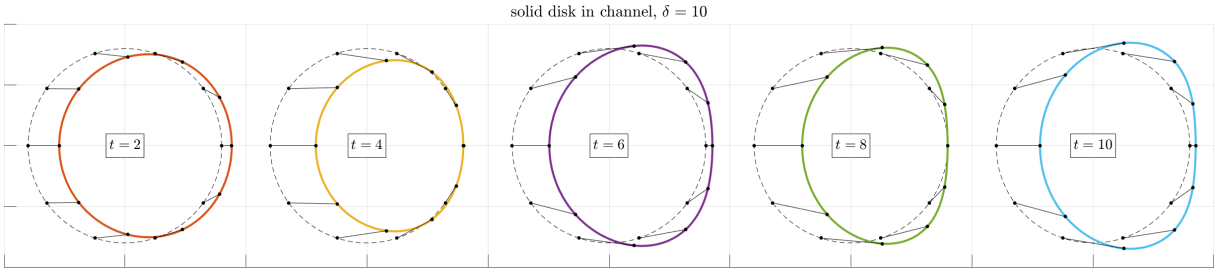

Figure 13: Position of the interface over time for the elastic annulus in a channel with density ratio $\delta = 10$, computed on grid $\mathcal{G}_d^{(8)}$. The displacement is magnified by 20 in this plot to accentuate the deformation.

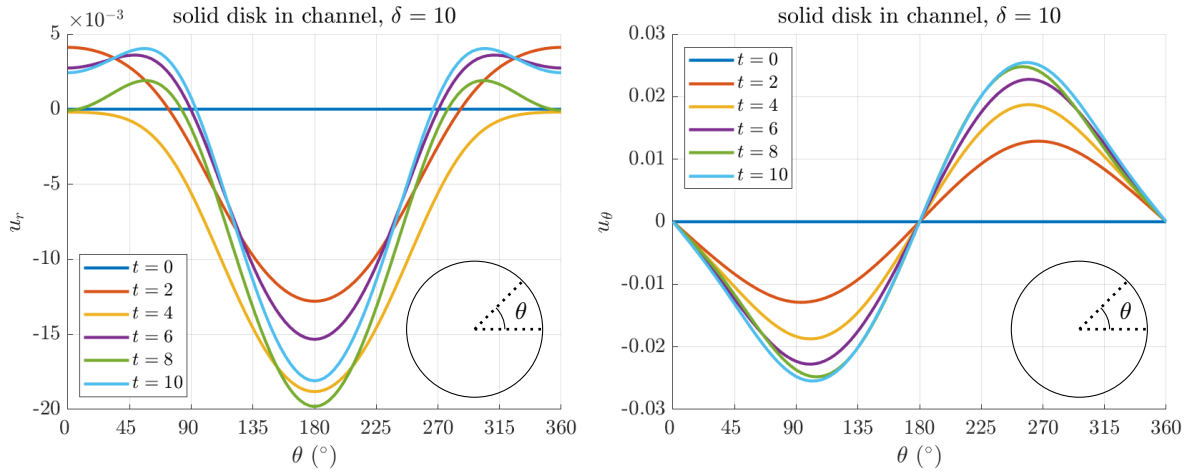

Figure 14: Radial (left) and circumferential (right) components of displacement as a function of the reference interface angle, θ, for the elastic annulus in a channel with density ratio $\delta = 10$, computed on grid $\mathcal{G}_d^{(8)}$.

To estimate the accuracy of the computed solution, a self-convergence test is performed and the results are presented in Table 3. Solutions are computed on the composite grids $\mathcal{G}_d^{(j)}$, $j = 2$, 4 and 8. The maximum error $E_j^{(\kappa)}$ in the solution component κ for grid $\mathcal{G}_d^{(j)}$, and the corresponding convergence rate, are estimated using a Richardson extrapolation procedure following the approach described in [49]. If the solution component is a vector (such as the velocity) or a tensor (such as the stress), then the error is taken as the maximum among all elements of the vector or tensor. The results in the table show that the max-norm errors are converging at close to second-order.

Elastic annulus in a channel, $\delta = 10$										
h_j	$E_j^{(p)}$	r	$E_j^{(\mathbf{v})}$	r	$E_j^{(\bar{\mathbf{u}})}$	r	$E_j^{(\bar{\mathbf{v}})}$	r	$E_j^{(\bar{\boldsymbol{\sigma}})}$	r
1/20	6.3e-3		7.4e-3		1.7e-4		4.1e-4		1.3e-2	
1/40	1.7e-3	3.7	1.5e-3	5.0	4.6e-5	3.7	9.2e-5	4.5	3.7e-3	3.6
1/80	4.7e-4	3.6	3.0e-4	4.9	1.2e-5	3.7	2.0e-5	4.5	1.0e-3	3.6
rate	1.86		2.30		1.90		2.18		1.86	

Table 3: Max-norm self-convergence results for the elastic annulus in a channel at $t = 1.5$ with density ratio $\delta = 10$.

Numerical solutions are also computed for this FSI problem using the traditional partitioned (TP) scheme. Table 4 shows the stability of the computed solution as a function of the density ratio $\delta = \bar{\rho}/\rho$ and the target grid spacing h for the composite grid $\mathcal{G}_d^{(j)}$. We observe that the TP scheme is unstable on even the coarsest grid used for $\delta = 200$ (and smaller) indicating that this value is already a *very light* solid case for the TP scheme. Larger values of δ are stable on the coarsest grid, but the results indicate that the TP scheme becomes unstable for a fixed value of δ as the grid is refined. This result is in agreement with the stability results discussed in [2] and [9].

h	$\delta = 100$	$\delta = 200$	$\delta = 300$	$\delta = 400$	$\delta = 500$	$\delta = 800$	$\delta = 1000$
1/20	unstable	unstable	stable	stable	stable	stable	stable
1/40	unstable	unstable	unstable	unstable	stable	stable	stable
1/80	unstable	unstable	unstable	unstable	unstable	unstable	stable

Table 4: Stability of the traditional-partitioned scheme for the elastic annulus in a channel as a function of the density ratio δ and the grid-spacing. Even for very heavy solids the TP scheme will become unstable when the grid becomes sufficiently fine.

5.5. Multiple elastic solids in a pressure-driven channel flow

To test the robustness of the AMP algorithm, we consider a final example of an incompressible fluid in a channel flowing past five embedded solids with different shapes and densities. The fluid has density $\rho = 1$ and viscosity $\nu = 0.02$, and it occupies the rectangular region $[-3.5, 5] \times [-2, 2]$. The form of the boundary conditions at the inlet and outlet of the channel, and along its top and bottom walls, are the same as that described for the pressure-driven flow in Section 5.4. For the present problem, the pressure is ramped smoothly from $p = 0$ at $t = 0$ to $p = p_0 = 0.1$ at $t = 0.5$ by prescribing $p(-3, y, t) = p_0\eta(2t)$ for $-2 < y < 2$ with the ramp function η given by (36).

Figure 15 describes the baseline reference geometries for the elastic solids $\bar{\Omega}_k$, $k = 1, \ldots, 5$, in the problem. These solids are positioned in the channel as shown in Figure 16. The geometric parameters that describe each solid are given in Table 5, along with the position (x_0, y_0) of the geometric center of each solid in the channel and the angle θ_0 of the solid (in degrees) relative to the baseline configurations shown in Figure 15. Each solid is anchored to the channel at a small circular hole of radius r_c and center (x_c, y_c) where the displacement is set to zero. We set $\bar{\rho} = \bar{\lambda} = \bar{\mu} = \delta$ for each solid with the different values for δ also listed in the table. The solid densities, which range from *very light*, $\delta = 0.1$, to very *heavy*, $\delta = 1000$, provide a significant test for a partitioned scheme. Also note that even large values for δ become difficult for the traditional scheme as the grids are refined as noted from Table 4.

The composite grid, denoted by $\mathcal{G}_{\text{mb}}^{(j)}$ with target grid spacing $\Delta s = 1/(10j)$, covers the fluid domain of the channel and reference domains of the five solids as shown in Figure 16. The fluid domain is composed of a (blue) background grid and a (green) deforming interface-fitted grid about each of the five solids. The (static) reference domain of each solid is composed of a (red)

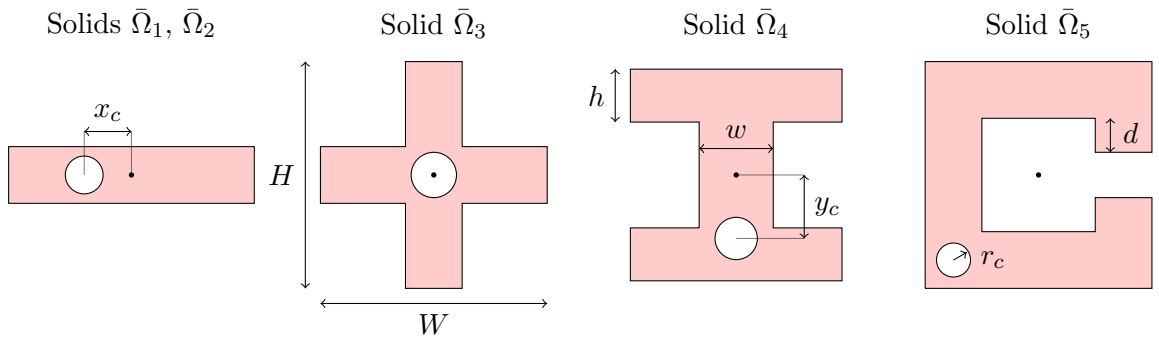

Figure 15: Geometry of the solids $\bar{\Omega}_k$, $k = 1, \ldots, 5$, in the channel flow. Each solid shape has an overall height H and width W, and may also be described by the parameters h and w corresponding to the height and width of rectangular segments as shown for $\bar{\Omega}_4$. The additional parameter d determines the height of the top and bottom vertical segments in $\bar{\Omega}_5$. Each solid includes a circular cut-out of radius r_c centered at (x_c, y_c) relative to the geometric center. Zero-displacement boundary conditions are applied on the cut-out to anchor each solid in the flow.

Solid	W	H	w	h	d	(x_c, y_c)	r_c	(x_0, y_0)	θ_0	δ
$\bar{\Omega}_1$	1.5	0.25	–	–	–	$(0.25, 0)$	0.05	$(-1.5, 0.85)$	$-10°$	2
$\bar{\Omega}_2$	1.5	0.35	–	–	–	$(-0.25, 0)$	0.05	$(-1.5, -1)$	$10°$	0.1
$\bar{\Omega}_3$	1.5	1.5	0.30	0.30	–	$(0, 0)$	0.1	$(0, 0)$	$20°$	1
$\bar{\Omega}_4$	1.0	1.0	0.35	0.25	–	$(0, -0.30)$	0.05	$(1.5, 0.75)$	$45°$	10
$\bar{\Omega}_5$	1.0	1.2	0.25	0.25	0.2	$(-0.35, -0.35)$	0.05	$(1.5, -0.85)$	$-160°$	1000

Table 5: Parameters for the solid objects in the channel as shown in Figure 16.

background grid, a (purple) interface-fitted grid, and a (pink) annular grid about the circular cut-out. An enlarged view of the composite grid showing more detail of the overlapping grid structure is also shown in the figure.

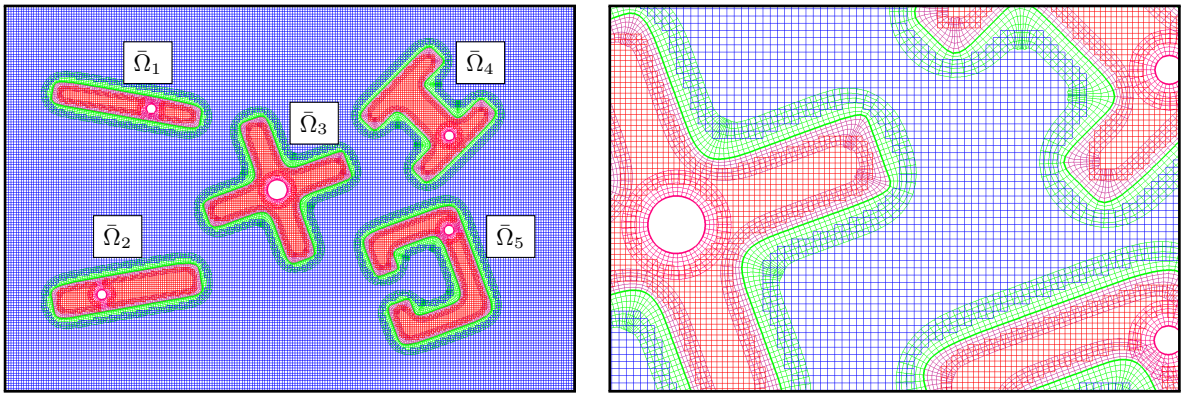

Figure 16: Left: composite grid $\mathcal{G}^{(4)}_{\text{mb}}$ for the multiple solid domains example. Right: zoomed in view of the composite grid $\mathcal{G}^{(4)}_{\text{mb}}$. Only the green fluid grids deform in time, all other grids are static.

Figure 17 shows computed results at two times, $t = 8$ and $t = 10$, with a comparison between two different grid resolutions, a 'coarse' grid $\mathcal{G}^{(4)}_{\text{mb}}$ (left column) and a 'fine' grid $\mathcal{G}^{(8)}_{\text{mb}}$ (right column). The plots in the figure show (instantaneous) streamlines in the fluid domain and shaded contours of the magnitude of displacement in each solid domain. The shaded contours are colored on different scales for each solid as noted in the figure caption. The streamlines are colored by the magnitude of the flow speed. The solids are seen to divert the flow with the fastest flow found above the

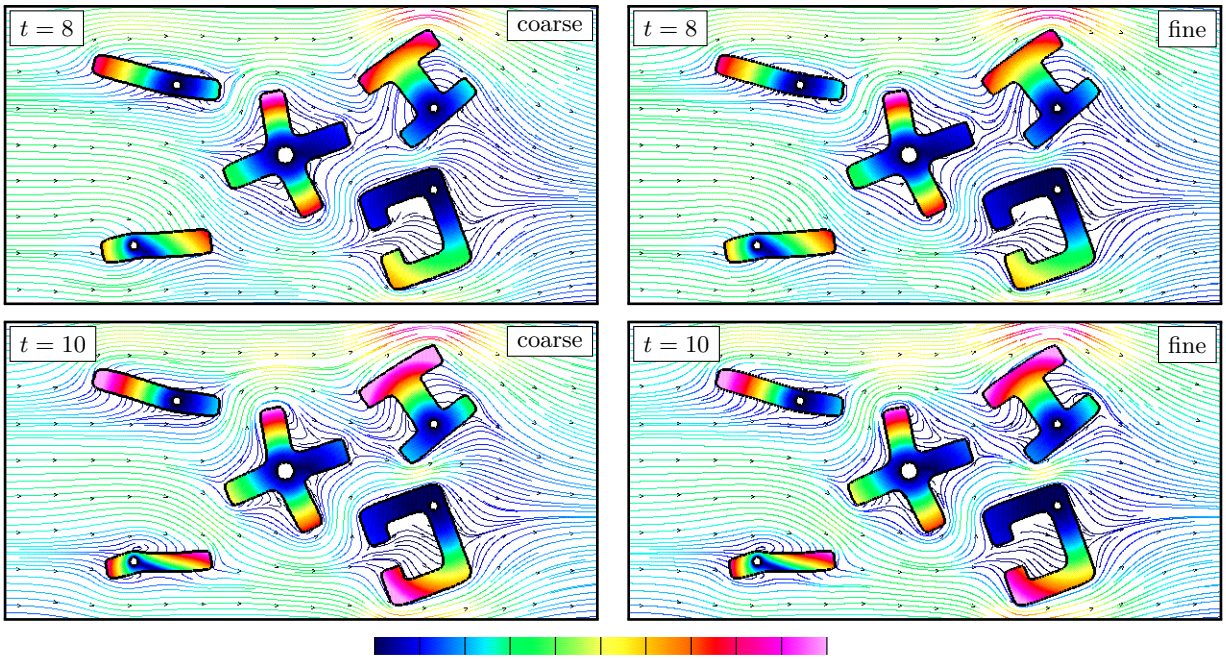

Figure 17: Plot of streamlines in the fluid and displacement norm in the solid at times $t = 8$ and $t = 10$ computed on coarse grid $\mathcal{G}_{\rm mb}^{(4)}$ (left) and fine grid $\mathcal{G}_{\rm mb}^{(8)}$ (right). The streamlines are coloured by the flow speed on a scale of $[0, 0.13]$. The contours of the displacement norm $|\bar{\mathbf{u}}|$ are coloured on a scale of $[0, \bar{U}_j]$ for body $\bar{\Omega}_j$ with $\bar{U}_1 = 0.1$, $\bar{U}_2 = 0.2$, $\bar{U}_3 = 0.09$, $\bar{U}_4 = 0.15$, and $\bar{U}_5 = 0.008$.

top of the I-shaped solid $\bar{\Omega}_4$. The flow is time-dependent and the solids undergo oscillations over time as elastic waves propagate through the bodies. The lighter solids are seen to deform more than the heavier ones. The rectangular beam $\bar{\Omega}_2$ at the bottom near the inlet of the channel, for example, is very light and is easily deformed by the fluid. As a result, it also undergoes a fairly large compression and expansion. Three arms of the plus-shaped solid $\bar{\Omega}_3$, are seen to be significantly pushed by the fluid while the top of the I-shaped solid is deformed to the right. Note that since the deformation of the bodies is time-dependent, the matching fluid velocity can be non-zero on the fluid-solid interfaces and the fluid streamlines appear to enter or exit the bodies at some locations. The results from the coarse and fine grid are very similar indicating a measure of grid convergence. Importantly, the AMP scheme is shown to be robust and stable for solid bodies with a wide range of densities.

6. Conclusions

An added-mass partitioned (AMP) algorithm was developed for fluid-structure interaction problems involving viscous incompressible flow and compressible elastic solids. The new algorithm was found to be stable and accurate, without sub-time-step iterations, for several difficult numerical tests involving both heavy and very light solids, thus illustrating that added-mass and added-damping effects were suppressed. Key elements of the new AMP scheme are a Robin interface condition for the pressure and an impedance-weighted interface projection based on a new form for the fluid impedance. The scheme was implemented in two dimensions using deforming composite grids to treat complex geometry with multiple deforming bodies. The fluid is advanced using a fractional-step IMEX scheme with the viscous terms treated implicitly, while the hyperbolic system for the solid is integrated using an explicit upwind scheme. Both domain solvers are individually

second-order accurate in both time and space. A number of new benchmark problems were developed including a *radial-piston* problem where exact solutions for radial and azimuthal motions were found. Traveling-wave exact solutions for a solid disk surrounded by an annulus of fluid were also derived. These exact solutions were used to verify the stability and second-order accuracy of the scheme. A clean benchmark problem involving a pressure-driven flow in a channel past a deformable solid annulus was developed and simulated; a self-convergence grid-refinement study was used to demonstrate second-order accuracy. A final example of flow past five solid bodies with densities ranging from 10^{-1} to 10^3 illustrated the flexibility and robustness of the new scheme.

While the new AMP algorithm has been shown to be accurate and stable, without sub-time-step iterations, for a variety of FSI problems involving both heavy and very light solids, there are opportunities available to extend the approach to a wider range of problems. For example, the AMP algorithm has been described for general three-dimensional problems, whereas the present study focused only on the implementation of the AMP algorithm in two space dimensions. Our experience in extending AMP algorithms for other FSI regimes to three dimensions (see [13] for example) suggests that there would be no essential difficulty in extending the implementation here to three dimensions. Another possible extension of the present work would be to elastic solids governed by nonlinear models. Such an extension was already considered by us for FSI problems involving inviscid compressible flow [18], and a similar extension could be undertaken for the case of viscous incompressible flow. Finally, many FSI problems involve stiff solids with large wave speeds. For such cases, it may be useful to consider multiple time-steps in the solid for every time-step of the fluid, or implicit time-stepping of the solid equations. These, and other extensions, will be considered in future work.

Appendix A. Radial piston exact solution

The geometry of a FSI problem involving radial motion of a circularly symmetric elastic piston is shown in Figure 6. An incompressible fluid occupies the annular region between the fluid-solid interface at $r = r_I(t)$ and an outer boundary at $r = R$. The fluid surrounds an elastic solid disk for $0 < r < r_I(t)$. It is assumed that the solid deforms in the radial direction only (as shown in the figure), and that the corresponding fluid motion is also confined to the radial direction. Under these assumptions, the fluid continuity equation (1a) in cylindrical coordinates reduces to

$$\frac{1}{r}\frac{\partial}{\partial r}(r v_r) = 0, \qquad r_I(t) < r < R,$$

so that the radial component of the fluid velocity is given by

$$v_r(r,t) = \frac{R}{r}V(t), \tag{A.1}$$

where $V(t)$ is the radial velocity of the fluid at $r = R$. The radial component of the momentum equation (1b) reduces to

$$\frac{\partial p}{\partial r} = \frac{\rho R^2}{r^3}V(t)^2 - \frac{\rho R}{r}\dot{V}(t), \qquad r_I(t) < r < R.$$

Integration with respect to r gives

$$p(r,t) = P(t) + \frac{\rho}{2}\left(1 - \frac{R^2}{r^2}\right)V(t)^2 + \rho R \log\left(\frac{R}{r}\right)\dot{V}(t), \tag{A.2}$$

where $P(t)$ is the fluid pressure at $r = R$. The evolution of the fluid velocity and pressure is completely determined by the interface position, $r_I(t)$, and the velocity and pressure at the outer radius, $V(t)$ and $P(t)$. These functions are found by matching the evolution of the fluid with that of the solid, which is considered next.

In the solid reference domain, the radial component of the momentum equation reduces to

$$\frac{\partial^2 \bar{u}_r}{\partial t^2} = \bar{c}_p^2 \frac{\partial}{\partial \bar{r}} \left(\frac{1}{\bar{r}} \frac{\partial}{\partial \bar{r}} \bar{r} \bar{u}_r \right), \qquad 0 < \bar{r} < r_0, \tag{A.3}$$

where $\bar{u}_r(\bar{r}, t)$ is the radial component of the solid displacement and $r_0 = r_I(0)$ is the initial radius of the interface. Bounded solutions of (A.3) as $\bar{r} \to 0$ are sought in the form

$$\bar{u}_r(\bar{r}, t) = \beta J_1(\omega \bar{r}/\bar{c}_p) \sin(\omega t), \tag{A.4}$$

where J_1 is the Bessel function of the first kind of order one, ω is the frequency of the oscillating displacement, and β determines the magnitude of the oscillation. In terms of the radial displacement in (A.4), the interface position in physical space is given by

$$r_I(t) = r_0 + \bar{u}_r(r_0, t) = r_0 + b \sin(\omega t), \qquad b = \beta J_1(\omega r_0/\bar{c}_p). \tag{A.5}$$

Matching the radial velocity of the fluid given in (A.1) to that of the solid determined from (A.4) on the interface gives

$$\frac{R}{r_I(t)} V(t) = \omega \beta J_1(\omega r_0/\bar{c}_p) \cos(\omega t) \tag{A.6}$$

which specifies $V(t)$. The matching condition on the radial component of stress is

$$-p(r, t) = \frac{\bar{\lambda}}{\bar{r}} \frac{\partial}{\partial \bar{r}} (\bar{r} \bar{u}_r) + 2\bar{\mu} \frac{\partial \bar{u}_r}{\partial \bar{r}}, \qquad r = r_I(t), \quad \bar{r} = r_0. \tag{A.7}$$

Using (A.2) and (A.4) in the stress condition (A.7) gives

$$\begin{aligned} -P(t) = \frac{\rho}{2} \left(1 - \frac{R^2}{r_I(t)^2} \right) V(t)^2 + \rho R \log \left(\frac{R}{r_I(t)} \right) \dot{V}(t) \\ + \beta \left[(\bar{\lambda} + 2\bar{\mu}) \frac{\omega}{\bar{c}_p} J_1'(\omega r_0/\bar{c}_p) + \frac{\bar{\lambda}}{r_0} J_1(\omega r_0/\bar{c}_p) \right] \sin(\omega t) \end{aligned} \tag{A.8}$$

An exact solution of the radial elastic piston problem is available based on the choice for the solid displacement in (A.4), which leads to the radial position of the fluid-solid interface given in (A.5). Matching the radial velocity and stress at the interface specifies $V(t)$ and $P(t)$ from (A.6) and (A.8), respectively, and these functions determine the fluid velocity and pressure given in (A.1) and (A.2).

Appendix B. Exact solution for the rotating elastic disk in a fluid annulus

An exact solution can be constructed for the case of circumferential motion of a circularly symmetric elastic disk. It is assumed that the radial components of the fluid velocity and the solid displacement are zero, and thus the interface is located at $r = r_0$ for all time. It is also assumed that the circumferential components of the fluid velocity, v_θ, and the solid displacement, $\bar{u}_\theta$, depend on r and t alone, so that the equations governing these quantities reduce to

$$\frac{\partial v_\theta}{\partial t} = \nu \frac{\partial}{\partial r} \left(\frac{1}{r} \frac{\partial}{\partial r} r v_\theta \right), \qquad r_0 < r < R, \tag{B.1}$$

and

$$\frac{\partial^2 \bar{u}_\theta}{\partial t^2} = \bar{c}_s^2 \frac{\partial}{\partial r}\left(\frac{1}{r}\frac{\partial}{\partial r} r\bar{u}_\theta\right), \qquad 0 < r < r_0, \tag{B.2}$$

respectively. Since there is no displacement in the radial direction, the reference coordinate, $\bar{r}$, is equivalent to the physical coordinate, r. Setting

$$v_\theta(r,t) = \hat{v}_\theta(r)e^{i\omega t}, \qquad \bar{u}_\theta(r,t) = \hat{\bar{u}}_\theta(r)e^{i\omega t}, \tag{B.3}$$

and substituting these into (B.1) and (B.2) it is found that the coefficient functions, $\hat{v}_\theta(r)$ and $\hat{\bar{u}}_\theta(r)$, both satisfy Bessel equations of order one. Assuming a no-slip boundary condition on the fluid velocity at $r = R$ and a bounded solution for the solid displacement as $r \to 0$, gives solutions of the form

$$\hat{v}_\theta(r) = b\big[J_1(\lambda r)Y_1(\lambda R) - J_1(\lambda R)Y_1(\lambda r)\big], \qquad \hat{\bar{u}}_\theta(r) = \bar{b}J_1(k_s r), \tag{B.4}$$

where J_1 and Y_1 are Bessel functions of the first and second kind, respectively. Here, $\lambda^2 = i\omega/\nu$, $k_s = \omega/\bar{c}_s$, and $(b, \bar{b})$ are constants. Matching conditions on velocity and stress imply

$$\hat{v}_\theta(r) = i\omega\hat{\bar{u}}_\theta(r), \qquad \mu\frac{d}{dr}\left(\frac{\hat{v}_\theta(r)}{r}\right) = \bar{\mu}\frac{d}{dr}\left(\frac{\hat{\bar{u}}_\theta(r)}{r}\right), \qquad \text{at } r = r_0. \tag{B.5}$$

Substituting (B.4) into the matching conditions in (B.5), and using the identity

$$\frac{d}{d\xi}\left(\frac{Z_1(\xi)}{\xi}\right) = -\frac{Z_2(\xi)}{\xi}, \qquad Z_n = J_n \text{ or } Y_n,$$

leads to the system

$$\begin{bmatrix} J_1(\lambda r_0)Y_1(\lambda R) - J_1(\lambda R)Y_1(\lambda r_0) & -i\omega J_1(k_s r_0) \\ -\mu\lambda\big[J_2(\lambda r_0)Y_1(\lambda R) - J_1(\lambda R)Y_2(\lambda r_0)\big] & \bar{\mu}k_s J_2(k_s r_0) \end{bmatrix} \begin{bmatrix} b \\ \bar{b} \end{bmatrix} = 0. \tag{B.6}$$

Nontrivial solutions for $(b, \bar{b})$ exist if the following determinant condition is met:

$$\begin{aligned} \mathcal{D}_2(\omega) = {} & \bar{\mu}k_s J_2(k_s r_0)\big[J_1(\lambda r_0)Y_1(\lambda R) - J_1(\lambda R)Y_1(\lambda r_0)\big] \\ & -i\omega\mu\lambda J_1(k_s r_0)\big[J_2(\lambda r_0)Y_1(\lambda R) - J_1(\lambda R)Y_2(\lambda r_0)\big]. \end{aligned} \tag{B.7}$$

Values of ω with $\Re(\omega) > 0$ satisfying $\mathcal{D}_2(\omega) = 0$ imply solutions of the rotating elastic disk problem that decay in time. For such a value of ω, a unique choice for $(b, \bar{b})$, satisfying (B.6), can be expressed as

$$\bar{b} = \frac{\bar{u}_0}{J_1(k_s r_0)}, \qquad b = \frac{i\omega\bar{u}_0}{J_1(\lambda r_0)Y_1(\lambda R) - J_1(\lambda R)Y_1(\lambda r_0)},$$

where $\bar{u}_0 = \bar{u}_\theta(r_0, 0)$ is the initial displacement of the interface. Solutions for the circumferential components of the fluid velocity and the solid displacement are taken from the real parts of $v_\theta(r,t)$ and $\bar{u}_\theta(r,t)$ given in (B.3), while the fluid pressure is given by

$$p(r,t) = \rho\int_{r_0}^{r} \frac{v_\theta(s,t)^2}{s}\, ds, \qquad r_0 < r < R,$$

assuming $p = 0$ on the interface $r = r_I(0) = r_0$.

Appendix C. Radial traveling wave solution

We consider traveling wave solutions of an FSI problem involving a Stokes fluid in the circular region $0 < r < r_0$ initially surrounded by a linearly elastic solid in the annular region $r_0 < r < R$. The solution is linearized about small interface deformations, therefore it is assumed that the interface is located at $r = r_0$ for all time.

In the fluid, solutions are sought of the form

$$v_r(r,\theta,t) = \hat{v}_r(r)e^{i(n\theta-\omega t)}, \qquad v_\theta(r,\theta,t) = \hat{v}_\theta(r)e^{i(n\theta-\omega t)}, \qquad p(r,\theta,t) = \hat{p}(r)e^{i(n\theta-\omega t)},$$

where ω is a frequency, n is a positive integer, and $\hat{v}_r(r)$, $\hat{v}_\theta(r)$ and $\hat{p}(r)$ are coefficient functions. Upon substitution, the equations governing the Stokes fluid become

$$\frac{1}{r}(r\hat{v}_r)' + \frac{in}{r}\hat{v}_\theta = 0, \tag{C.1}$$

$$-i\omega\rho\hat{v}_r + \hat{p}' = \mu\left(\frac{1}{r}(r\hat{v}_r')' - \frac{n^2}{r^2}\hat{v}_r - \frac{\hat{v}_r}{r^2} - \frac{2in}{r^2}\hat{v}_\theta\right), \tag{C.2}$$

$$-i\omega\rho\hat{v}_\theta + \frac{in}{r}\hat{p}' = \mu\left(\frac{1}{r}(r\hat{v}_\theta')' - \frac{n^2}{r^2}\hat{v}_\theta + \frac{2in}{r^2}\hat{v}_r - \frac{\hat{v}_\theta}{r^2}\right). \tag{C.3}$$

An elliptic equation for the pressure can be obtained from (C.1)–(C.3), and it takes the form

$$\hat{p}'' + \frac{1}{r}\hat{p}' - \frac{n^2}{r^2}\hat{p} = 0. \tag{C.4}$$

Bounded solutions of the Cauchy-Euler equation in (C.4) at $r = 0$ are

$$\hat{p}(r) = p_I\left(\frac{r}{r_0}\right)^n,$$

where p_I is a constant corresponding to the pressure at the (linearized) fluid-solid interface. Using (C.1) to eliminate $\hat{v}_\theta$ from (C.2) gives

$$r^2\hat{v}_r'' + 3r\hat{v}_r' + (\lambda^2r^2 - n^2 + 1)\hat{v}_r = p_I\frac{nr^{n+1}}{\mu r_0^n}, \tag{C.5}$$

where $\lambda^2 = i\omega/\nu$. Bounded solutions of (C.5) at $r = 0$ have the form

$$\hat{v}_r(r) = d\frac{J_n(\lambda r)}{r} + p_I\frac{nr^{n-1}}{\mu\lambda^2 r_0^n},$$

where d is a constant and $J_n(z)$ is the Bessel function of the first kind of order n. The corresponding solution for $\hat{v}_\theta$, obtained from (C.1), is given by

$$\hat{v}_\theta(r) = d\frac{i\lambda}{n}J_n'(\lambda r) + p_I\frac{inr^{n-1}}{\mu\lambda^2 r_0^n}.$$

In the solid, we consider the solid displacement in the form

$$\bar{\mathbf{u}} = \nabla\phi + \nabla\times\mathbf{H}, \tag{C.6}$$

where ϕ is a potential and $\mathbf{H}$ is a vector field. Let $\mathbf{e}_r = [\cos\theta, \sin\theta, 0]^T$, $\mathbf{e}_\theta = [-\sin\theta, \cos\theta, 0]^T$, and $\mathbf{e}_z = [0,0,1]^T$ represent the polar basis. Since we are interested in displacements in the two-dimensional (r,θ) plane, we take $\mathbf{H} = H\mathbf{e}_z$. With these assumptions, the equations governing linear

elasticity reduce to a longitudinal and shear wave equations for $\phi(r,\theta,t)$ and $H(r,\theta,t)$, respectively, having the form

$$\frac{\partial^2\phi}{\partial t^2} = \bar{c}_p^2\left(\frac{1}{r}\frac{\partial}{\partial r}\left(r\frac{\partial\phi}{\partial r}\right)+\frac{1}{r^2}\frac{\partial^2\phi}{\partial\theta^2}\right), \qquad \frac{\partial^2 H}{\partial t^2} = \bar{c}_s^2\left(\frac{1}{r}\frac{\partial}{\partial r}\left(r\frac{\partial H}{\partial r}\right)+\frac{1}{r^2}\frac{\partial^2 H}{\partial\theta^2}\right). \tag{C.7}$$

As before, we seek solutions of the form

$$\phi(r,\theta,t) = \hat{\phi}(r)e^{i(n\theta-\omega t)}, \qquad H(r,\theta,t) = \hat{H}(r)e^{i(n\theta-\omega t)}.$$

Upon substitution into (C.7), we find

$$r^2\hat{\phi}'' + r\hat{\phi} + \left((k_p r)^2 - n^2\right)\hat{\phi} = 0, \qquad r^2\hat{H}'' + r\hat{H} + \left((k_s r)^2 - n^2\right)\hat{H} = 0, \tag{C.8}$$

where $k_p = \omega/\bar{c}_p$ and $k_s = \omega/\bar{c}_s$. General solutions of the two equations in (C.8) involve Bessel functions of the first and second kinds, and are given by

$$\hat{\phi}(r) = \bar{d}_1 J_n(k_p r) + \bar{d}_2 Y_n(k_p r), \qquad \hat{H}(r) = \bar{d}_3 J_n(k_s r) + \bar{d}_4 Y_n(k_s r),$$

where $(\bar{d}_1,\bar{d}_2,\bar{d}_3,\bar{d}_4)$ are constants. Using (C.6), the coefficient functions for the solid displacements in the radial and circumferential directions are given by

$$\hat{\bar{u}}_r(r) = \hat{\phi}' + \frac{in}{r}\hat{H}, \qquad \hat{\bar{u}}_\theta(r) = \frac{in}{r}\hat{\phi} - \hat{H}',$$

respectively. For later purposes, we also require coefficient functions for the stress components $(\bar{\sigma}_{rr},\bar{\sigma}_{r\theta})$ in terms of $\hat{\phi}$ and $\hat{H}$, which are given by

$$\hat{\bar{\sigma}}_{rr}(r) = (2\bar{\mu}+\bar{\lambda})\hat{\phi}'' + \frac{\bar{\lambda}}{r}\left(\hat{\phi}' - \frac{n^2}{r}\hat{\phi}\right) + \frac{2i\bar{\mu}n}{r}\left(\hat{H}' - \frac{1}{r}\hat{H}\right),$$
$$\hat{\bar{\sigma}}_{r\theta}(r) = -\bar{\mu}\hat{H}'' + \frac{\bar{\mu}}{r}\left(\hat{H}' - \frac{n^2}{r}\hat{H}\right) + \frac{2i\bar{\mu}n}{r}\left(\hat{\phi}' - \frac{1}{r}\hat{\phi}\right).$$

The solution for the fluid involves the two constants (p_I, d), while the solution for the solid involves the four constants $(\bar{d}_1,\bar{d}_2,\bar{d}_3,\bar{d}_4)$. Constraints for these six constants can be obtained by imposing boundary conditions on the solid at $r = R$ and the matching conditions at the fluid-solid interface, $r = r_0$. At the outer boundary of the solid, we assume traction-free boundary conditions of the form

$$\hat{\bar{\sigma}}_{rr}(R) = \hat{\bar{\sigma}}_{r\theta}(R) = 0, \tag{C.9}$$

while matching conditions on the velocity and stress at the interface give

$$\hat{v}_r(r_0) = -i\omega\hat{\bar{u}}_r(r_0), \quad \hat{v}_\theta(r_0) = -i\omega\hat{\bar{u}}_\theta(r_0), \quad \hat{\sigma}_{rr}(r_0) = \hat{\bar{\sigma}}_{rr}(r_0), \quad \hat{\sigma}_{r\theta}(r_0) = \hat{\bar{\sigma}}_{r\theta}(r_0). \tag{C.10}$$

The two constraints in (C.9) with the four constraints in (C.10) lead to a homogeneous system of equations of the form

$$M\mathbf{d} = 0,$$

for the vector of constants $\mathbf{d} = [p_I, d, \bar{d}_1, \bar{d}_2, \bar{d}_3, \bar{d}_4]^T$. Nontrivial solutions for $\mathbf{d}$ exist if $\det(M) = 0$, which leads to a dispersion relation between the frequency ω and the circumferential wave number n of the form

$$\mathcal{F}(n,\omega) = 0. \tag{C.11}$$

For a given (n,ω)-pair satisfying (C.11), a nontrivial $\mathbf{d}$ can be found subject to the normalization

$$\|\bar{\mathbf{u}}(r_0,0,0)\|^2 = \bar{u}_r(r_0,0,0)^2 + \bar{u}_\theta(r_0,0,0)^2 = \bar{u}_0^2,$$

where $\bar{u}_0$ is an initial displacement of the interface. Solutions of (C.11) for (n,ω) and the corresponding constants in $\mathbf{d}$ are given in Section 5.3 for the case $\bar{u}_0 = 10^{-7}$.

References

[1] P. Causin, J. F. Gerbeau, F. Nobile, Added-mass effect in the design of partitioned algorithms for fluid–structure problems, Comput. Method. Appl. Mech. Engrg. 194 (2005) 4506–4527.

[2] J. W. Banks, W. D. Henshaw, D. W. Schwendeman, An analysis of a new stable partitioned algorithm for FSI problems. Part I: Incompressible flow and elastic solids, J. Comput. Phys. 269 (2014) 108–137.

[3] J. W. Banks, W. D. Henshaw, D. W. Schwendeman, An analysis of a new stable partitioned algorithm for FSI problems. Part II: Incompressible flow and structural shells, J. Comput. Phys. 268 (2014) 399–416.

[4] L. Li, W. D. Henshaw, J. W. Banks, D. W. Schwendeman, G. A. Main, A stable partitioned FSI algorithm for incompressible flow and deforming beams, J. Comput. Phys. 312 (2016) 272–306.

[5] J. W. Banks, W. D. Henshaw, D. W. Schwendeman, Deforming composite grids for solving fluid structure problems, J. Comput. Phys. 231 (9) (2012) 3518–3547.

[6] W. D. Henshaw, D. W. Schwendeman, Moving overlapping grids with adaptive mesh refinement for high-speed reactive and non-reactive flow, J. Comput. Phys. 216 (2) (2006) 744–779.

[7] D. Appelö, J. W. Banks, W. D. Henshaw, D. W. Schwendeman, Numerical methods for solid mechanics on overlapping grids: Linear elasticity, J. Comput. Phys. 231 (18) (2012) 6012–6050.

[8] W. D. Henshaw, N. A. Petersson, A split-step scheme for the incompressible Navier-Stokes equations, in: M. M. Hafez (Ed.), Numerical Simulation of Incompressible Flows, World Scientific, 2003, pp. 108–125.

[9] D. A. Serino, J. W. Banks, W. D. Henshaw, D. W. Schwendeman, A stable added-mass partitioned (AMP) algorithm for elastic solids and incompressible flow: Model problem analysis, SIAM J. Sci. Comput.(to appear).

[10] D. A. Serino, J. W. Banks, W. D. Henshaw, D. W. Schwendeman, A stable added-mass partitioned (AMP) algorithm for elastic solids and incompressible flow: Model problem analysis, preprint arXiv:1812.03192, submitted for publication (2019).

[11] J. W. Banks, W. D. Henshaw, D. W. Schwendeman, Q. Tang, A stable partitioned FSI algorithm for rigid bodies and incompressible flow. Part I: Model problem analysis., J. Comput. Phys. 343 (2017) 432–468.

[12] J. W. Banks, W. D. Henshaw, D. W. Schwendeman, Q. Tang, A stable partitioned FSI algorithm for rigid bodies and incompressible flow. Part II: General formulation, J. Comput. Phys. 343 (2017) 469–500.

[13] J. W. Banks, W. D. Henshaw, D. W. Schwendeman, Q. Tang, A stable partitioned FSI algorithm for rigid bodies and incompressible flow in three dimensions, J. Comput. Phys. 373 (2018) 455–492.

[14] J. W. Banks, B. Sjögreen, A normal mode stability analysis of numerical interface conditions for fluid/structure interaction, Commun. Comput. Phys. 10 (2) (2011) 279–304.

[15] B. Sjögreen, J. W. Banks, Stability of finite diference discretizations of multi-physics interface conditions, Commun. Comput. Phys. 13 (2013) 386–410.

[16] E. H. van Brummelen, Added mass effects of compressible and incompressible flows in fluid–structure interaction, J. Appl. Mechanics 76 (2) (2009) 021206–021212.

[17] J. W. Banks, W. D. Henshaw, B. Sjögreen, A stable FSI algorithm for light rigid bodies in compressible flow, J. Comput. Phys. 245 (2013) 399–430.

[18] J. W. Banks, W. D. Henshaw, A. Kapila, D. W. Schwendeman, An added-mass partitioned algorithm for fluid-structure interactions of compressible fluids and nonlinear solids, J. Comput. Phys. 305 (2016) 1037–1064.

[19] G. Guidoboni, R. Glowinski, N. Cavallini, S. Čanić, Stable loosely-coupled-type algorithm for fluid–structure interaction in blood flow, J. Comput. Phys. 228 (18) (2009) 6916–6937.

[20] M. Bukač, S. Čanič, R. Glowinski, J. Tambača, A. Quaini, Fluid–structure interaction in blood flow capturing non-zero longitudinal structure displacement, J. Comput. Phys. 235 (2013) 515–541.

[21] M. Bukač, S. Čanič, B. Muha, A partitioned scheme for fluid–composite structure interaction problems, Journal of Computational Physics 281 (2015) 493 – 517.

[22] U. Küttler, W. A. Wall, Fixed-point fluid–structure interaction solvers with dynamic relaxation, Computational Mechanics 43 (1) (2008) 61–72.

[23] M. Mehl, B. Uekermann, H. Bijl, D. Blom, B. Gatzhammer, A. van Zuijlen, Parallel coupling numerics for partitioned fluid-structure interaction simulations, Computers & Mathematics with Applications 71 (4) (2016) 869 – 891.

[24] Y. Wang, A. Quaini, S. Čanić, A higher-order discontinuous Galerkin/arbitrary Lagrangian Eulerian partitioned approach to solving fluid–structure interaction problems with incompressible, viscous fluids and elastic structures, Journal of Scientific Computing 76 (1) (2018) 481–520.

[25] S. Basting, A. Quaini, S. Čanić, R. Glowinski, Extended ALE method for fluid-structure interaction problems with large structural displacements, Journal of Computational Physics 331 (2017) 312 – 336.

[26] S. Badia, F. Nobile, C. Vergara, Fluid–structure partitioned procedures based on Robin transmission conditions, J. Comput. Phys. 227 (14) (2008) 7027–7051.

[27] D. P. Mok, W. A. Wall, E. Ramm, Accelerated iterative substructuring schemes for instationary fluid structure interaction, in: K. Bathe (Ed.), Computational Fluid and Solid Mechanics, Elsevier, 2001, pp. 1325–1328.

[28] M. A. Fernández, J. Mullaert, M. Vidrascu, Generalized Robin-Neumann explicit coupling schemes for incompressible fluid–structure interaction: stability analysis and numerics, Int. J. Numer. Meth. Eng. .

[29] M. A. Fernández, J. Mullaert, M. Vidrascu, Explicit Robin-Neumann schemes for the coupling of incompressible fluids with thin-walled structures, Comput. Method. Appl. Mech. Engrg. 267 (2013) 566–593.

[30] M. A. Fernández, M. Landajuela, Fully decoupled time-marching schemes for incompressible fluid/thin-walled structure interaction, Rapport de recherche RR-8425, INRIA (Jan. 2014).

[31] L. Gerardo-Giorda, F. Nobile, C. Vergara, Analysis and optimization of Robin-Robin partitioned procedures in fluid–structure interaction problems, SIAM J. Numer. Anal. 48 (6) (2010) 2091–2116.

[32] S. Badia, F. Nobile, C. Vergara, Robin-Robin preconditioned Krylov methods for fluid–structure interaction problems, CMAME 198 (33–36) (2009) 2768–2784.

[33] F. Nobile, M. Pozzoli, C. Vergara, Inexact accurate partitioned algorithms for fluid–structure interaction problems with finite elasticity in haemodynamics, Journal of Computational Physics 273 (0) (2014) 598 – 617.

[34] H. Baek, G. E. Karniadakis, A convergence study of a new partitioned fluid–structure interaction algorithm based on fictitious mass and damping, J. Comput. Phys. 231 (2) (2012) 629–652.

[35] Y. Yu, H. Baek, G. E. Karniadakis, Generalized fictitious methods for fluid–structure interactions: Analysis and simulations, J. Comput. Phys. 245 (2013) 317–346.

[36] P. Raback, J. Ruokolainen, M. Lyly, Fluid–structure interaction boundary conditions by artificial compressibility, in: ECCOMAS Computational Fluid Dynamics Conference 2001 Swansea, Wales, UK, 2001, pp. 4–7.

[37] J. Degroote, A. Swillens, P. Bruggeman, R. Haelterman, P. Segers, J. Vierendeels, Simulation of fluid–structure interaction with the interface artificial compressibility method, Int. J. Numer. Meth. Bio. Engrg. 26 (3-4) (2010) 276–289.

[38] J. Degroote, On the similarity between Dirichlet-Neumann with interface artificial compressibility and Robin-Neumann schemes for the solution of fluid–structure interaction problems, J. Comput. Phys. 230 (17) (2011) 6399–6403.

[39] M. A. Fernández, J.-F. Gerbeau, C. Grandmont, A projection semi-implicit scheme for the coupling of an elastic structure with an incompressible fluid, Int. J. Numer. Meth. Eng. 69 (4) (2007) 794–821.

[40] D. Forti, M. Bukac, A. Quaini, S. Canic, S. Deparis, A monolithic approach to fluid–composite structure interaction, Journal of Scientific Computing 72 (1) (2017) 396–421.

[41] C. A. Figueroa, I. E. Vignon-Clementel, K. E. Jansen, T. J. Hughes, C. A. Taylor, A coupled momentum method for modeling blood flow in three-dimensional deformable arteries, Comput. Method. Appl. Mech. Engrg. 195 (41-43) (2006) 5685–5706.

[42] E. Aulisa, S. Bnà, G. Bornia, A monolithic ALE Newton-Krylov solver with multigrid-Richardson-Schwarz preconditioning for incompressible fluid-structure interaction, Computers & Fluids 174 (2018) 213 – 228.

[43] M. Heil, An efficient solver for the fully coupled solution of large-displacement fluid–structure interaction problems, Comput. Method. Appl. Mech. Engrg. 193 (1–2) (2004) 1 – 23.

[44] M. W. Gee, U. Küttler, W. A. Wall, Truly monolithic algebraic multigrid for fluid–structure interaction, Int. J. Numer. Meth. Eng. 85 (2011) 987–1016.

[45] J. Hron, S. Turek, A monolithic FEM/multigrid solver for an ALE formulation of fluid–structure interaction with applications in biomechanics, in: Bungartz, Schäfer (Eds.), Fluid–Structure Interaction, Springer, 2006, pp. 146–170.

[46] W. D. Henshaw, Ogen: An overlapping grid generator for Overture, Research Report UCRL-MA-132237, Lawrence Livermore National Laboratory (1998).

[47] W. D. Henshaw, The Overture hyperbolic grid generator, user guide, version 1.0, Research Report UCRL-MA-134240, Lawrence Livermore National Laboratory (1999).

[48] W. D. Henshaw, A fourth-order accurate method for the incompressible Navier-Stokes equations on overlapping grids, J. Comput. Phys. 113 (1) (1994) 13–25.

[49] W. D. Henshaw, D. W. Schwendeman, Parallel computation of three-dimensional flows using overlapping grids with adaptive mesh refinement, J. Comput. Phys. 227 (16) (2008) 7469–7502.